Contrib Mineral Petrol (2006) 151: 457–479
DOI 10.1007/s00410-006-0071-x

ORIGINAL PAPER

Jianping Zheng · W. L. Griffin · Suzanne Y. O'Reilly
Ming Zhang · Norman Pearson · Zhaohua Luo

The lithospheric mantle beneath the southwestern Tianshan area, northwest China

Received: 9 August 2005 / Accepted: 25 January 2006 / Published online: 11 March 2006

Abstract A suite of spinel peridotite xenoliths in Mesozoic basalts of the Tuoyun basin in the Tianshan area of northwest China has a high proportion of amphibole/mica-bearing lherzolites, with high Cpx/Opx ratios (mean 0.74). Many aspects of mineral chemistry in the Tuoyun peridotites are intermediate between those of refractory Archean cratonic mantle and fertile Phanerozoic mantle. These include Ni/Cr and the contents of transition metals and Y in olivine and orthopyroxene and the abundances of elements such as Na, Al, Ti, Y, Sr and LREE in clinopyroxene. The data suggest that the mantle in Tuoyun is moderately depleted in basaltic components relative to both the refractory Archean mantle and the fertile Phanerozoic mantle. The wide variations in the CaO/Al_2O_3 (0.9–3.5) of whole rocks and LREE/HREE (0.8–14.2) and Ti/Eu (971–5,765) of clinopyroxenes in the Tuoyun peridotites are interpreted as the metasomatism of hydrous carbonatitic and potassic melt or the cumulative effects of mantle metasomatism by different agents (carbonatite and small-volume silicate melts) through time. The Tuoyun mantle shows closer affinity to the type of mantle found beneath the Proterozoic Cathaysia block, and especially to that beneath the East Central Asia Orogenic Belt (ECAOB), than to the mantle beneath the Archean North China Craton. This implies that the Tianshan subcontinental lithospheric mantle may have been generated during the accretion of the ECAOB. The high proportion of fine-grained microstructures, high Cpx/Opx ratio, obvious Ca enrichment and lower overall depletion in the Tuoyun mantle relative to that in other parts of the ECAOB reflect stronger mechanical and chemical modification of the Tuoyun mantle, near the translithospheric Talas-Ferghana strike-slip fault, which played a major role in controlling the strength of the mantle lithosphere and has channeled the upwelling mantle.

Communicated by T. L. Grove

J. Zheng (✉)
State Key Laboratory of Geological Processes and Mineral Resources, Faculty of Earth Sciences, China University of Geosciences, Wuhan 430074, China
E-mail: jpzheng@cug.edu.cn
Tel.: +86-27-67883873
Fax: +86-27-67883002

W. L. Griffin · S. Y. O'Reilly · M. Zhang · N. Pearson · J. Zheng
GEMOC ARC National Key Centre, Department of Earth and Planetary Sciences, Macquarie University, Sydney, NSW 2109, Australia
E-mail: bill.griffin@mq.edu.au
E-mail: sue.oreilly@mq.edu.au
E-mail: ming.zhang@mq.edu.au
E-mail: npearson@mq.edu.au

W. L. Griffin
CSIRO Exploration and Mining, Sydney, NSW 2113, Australia

Z. Luo
State Key Laboratory of Geological Processes and Mineral Resources, China University of Geosciences, Beijing 100083, China
E-mail: luozh@cugb.edu.cn

Introduction

The East Central Asia Orogenic Belt (ECAOB) is a major Phanerozoic orogen located between the Siberian craton in the north and several smaller cratons (including the North China Craton) in the south. Recent research (e.g., Sengör and Natal'in 1996; Zorin 1999; Ionov 2002) indicates that this orogenic belt had a complicated history involving Phanerozoic subduction of oceanic crust, closure of paleo-oceans and prolonged extensive silicic magmatism. Precambrian continental fragments (or microcontinents) are preserved in many parts of the orogenic belt. However, the nature and evolution of the subcontinental lithospheric mantle (SCLM) beneath this huge (≥1,000 km wide) orogenic belt is little known. Mantle-derived xenoliths in alkali basalts provide spot samples of the SCLM at several locations across the ECAOB, such as the Wudalianchi-Erkeshan-Keluo (WEK) areas (Fig. 1a; Zhang et al. 2000), the Vitim plateau (Glaser et al. 1999; Litasov

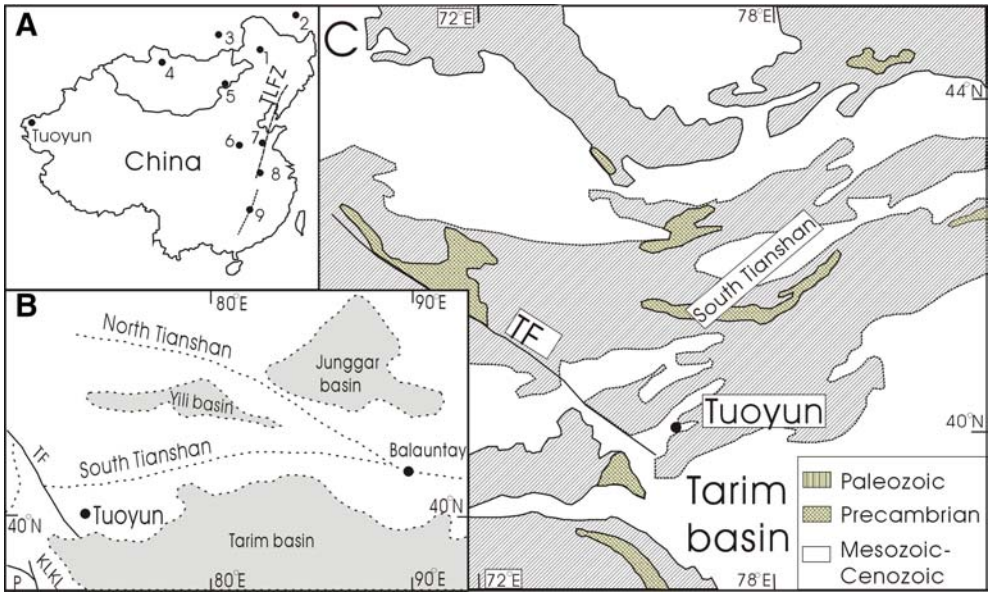

Fig. 1 Locality maps. **a** Selected localities of peridotitic xenoliths from eastern China, central-eastern Mongolia and eastern Siberia: *1* Wudalianchi-Erkeshan-Keluo (WEK, China), *2* Vitim, *3* Sikhote-Alin (Siberia), *4* Tariat (Mongolia), *5* Dariganga (China–Mongolia) from the eastern part of the Phanerozoic Central Asian Fold Belt, *6* Hebi, *7* Shanwang, *8* Nushan from the Archean North China Craton, *9* Daoxian from the Proterozoic Cathaysia Craton. Shanwang, Nushan and Daoxian are associated with deep translithospheric faults (TLFZ). **b**, **c** Tuoyun and schematic map of central Asia showing subdivision of the Tianshan area; *TF* Talas-Ferghana strike-slip fault, *P* Pamir, *KLKL* Karakunlun Mountains. Modified after Brookfield (2000)

et al. 2000; Ionov et al. 2005), Sikhote-Alin (Ionov et al. 1995), the Tariat region (Kopylova et al. 1995; Ionov et al. 1997) and the Dariganga lava plateau (Wiechert et al. 1997; Ionov et al. 1999; Ionov 2002). However, all of these localities are from the eastern part of the belt, and there are no reports on mantle xenoliths from the western part of the orogen.

The Tianshan (Tien Shan) Mountains extend east–west for at least 2,500 km in central Asia, from Uzbekistan, Tajikistan and Kirghizia to northwest China, regarded as an active part of the Indian–Asian collision system. Previous studies on the Tianshan and adjacent regions mainly concentrated on the Paleozoic collisional tectonics and evolution (e.g., Windley et al. 1990; Allen et al. 1992; Shi et al. 1994; Gao et al. 1995, 1998; Chen et al. 1999), Mesozoic–Cenozoic intracontinent basin evolution (e.g., Carroll et al. 1990; Graham et al. 1990; Allen et al. 1991; Hendrix et al. 1992, 1994) and neotectonics (e.g., Molnar and Tapponnier 1975; Tapponnier and Molnar 1979; Nelson et al. 1987; Chen et al. 2002). It is broadly accepted that the Tianshan is a complex Paleozoic orogen with composite terrains (e.g., Coleman 1989; Windley et al. 1990) and began to be uplifted with accompanying volcanic eruption and granite intrusion in the early Permian. The uplift accelerated in the late Permian and continental molasse was extensively deposited (Afonichev and Vlasov 1984). Since late Permian time, the Tianshan has largely experienced a period of magmatic quiescence.

An exception is a volumetrically small series of basaltic rocks erupted primarily in Mesozoic-Paleogene sedimentary rocks, such as in the Tuoyun (Tuyon) basin of NW China and in the central portion of the Kyrgyz Tianshan (Dobresov and Zagruzina 1977; Afonichev and Vlasov 1984; Zhou and Zheng 1992; Han et al. 1998). These basaltic rocks have ocean island basalt (OIB)-like geochemistry and may be related to the activity of a small mantle plume (Sobel and Arnaud 2000). However, the lack of direct evidence from xenoliths has hindered our understanding of the nature of the lithospheric mantle in this region.

Peridotite xenoliths recently collected from Cretaceous basalts in the Tuoyun basin, a locality near the Talas-Ferghana (TF) strike-slip fault (Fig. 1b, c), offer a unique glimpse into the nature of the lithospheric upper mantle beneath the Tianshan. Here we present detailed petrographic and mineral chemistry data, including the major and trace elements, for these xenoliths. Our aims are to characterize the nature of the lithospheric mantle beneath the Tianshan in Mesozoic time, to compare it to the mantle beneath other cratonic and noncratonic regions of China and to use these data to understand the generation of the lithosphere beneath this complex orogen.

Geological setting

The Tianshan orogenic belt is one of the most important Paleozoic orogens in central Asia. In NW China, the orogenic belt includes parts of the Tarim and Yili-Central Tianshan blocks, which are microcontinental fragments with Precambrian basement and Mesozoic–Cenozoic cover (Fig. 1b). The Tarim block is separated

from the Yili-Central Tianshan block by the southern Central Tianshan suture (Early Carboniferous). Ophiolitic mélanges and blueschists are widespread in this suture zone and are believed to have been produced by the collision between a passive continental margin on the north side of the Tarim block and an active continental margin on the south side of the Yili-Central Tianshan block at the end of Early Carboniferous (Gao et al. 1998). The Tianshan can be subdivided into three portions along its length: the eastern section is located in Chinese territory, east of the lake Issyk Kul; the central section extends west to the TF strike-slip fault; the western section extends west from this fault. West of Balguntay, the Tianshan is split into northern and southern branches separated by the Yili Basin. Paleo- to Mesoproterozoic basement rocks occur widely in the uplifted zones from east to west Tianshan.

In the Western Tianshan, Precambrian metamorphic rocks have been recently dated at 1900–707 Ma (Hu et al. 1997, 2000; Chen et al. 1999, 2000). In the Eastern Tianshan, early Paleozoic strata are relatively minor in comparison with late Paleozoic sequences including island arc volcanic rocks, volcaniclastic and some marine sedimentary rocks. The broad distribution of ophiolites has been used to delineate paleo-sutures (Windley et al. 1990). Granitic rocks are widespread in the Tianshan region. Most of them have late Paleozoic ages (ca. 300 Ma) and a few were emplaced during early Paleozoic (450–400 Ma) or Neoproterozoic time (1200–960 Ma; Hu et al. 1986). The paleo-ocean of south Tianshan closed after the Devonian and essential accretion took place at ca. 360 Ma (Xiao et al. 1992; Chen et al. 1999). Intense intracontinental orogeny, manifested by postcollisional uplifts and simultaneous subsidence of major basins (e.g., Tarim, Junggar and Turpan), took place since the early Permian (e.g., Windley et al. 1990). In the late Permian, the uplift accelerated, accompanied by the deposition of extensive continental molasse.

The Tuoyun basin is located in the southern central Tianshan of NW China and the central portion of the Kyrgyz Tianshan (Afonichev and Vlasov 1984) and preserves a small volume of basalts, primarily interbedded with Mesozoic-Paleogene sedimentary rocks. The basalts are OIB-like in geochemical character and yield $^{40}Ar/^{39}Ar$ ages of 120–110 and 67–46 Ma (Sobel and Arnaud 2000). The peridotite xenoliths in this study were collected from the lowest part of the basalts in the Tuoyun basin, at a locality 1 km south of Tuoyun County (40°9.50′N and 75°20.54′E). They are accompanied by abundant granulite (Zheng et al. 2006) and pyroxenite xenoliths and megacrysts (up to 9 cm long) of amphibole, pyroxene and anorthoclase.

Studies on peridotite xenoliths from eastern China and the ECAOB provide a baseline for geochemical comparisons between the Tuoyun mantle peridotites and those from some basalt provinces in eastern China, central-eastern Mongolia and eastern Siberia (Fig. 1a). The Hebi, Qixia, Shanwang and Nushan localities are on the Archean North China Craton, and the Daoxian, Anyuan, Mingxi, Qilin and Niutuoshan localities are from the Proterozoic Cathaysia Block. Among the suites from Precambrian terrains, the Shanwang, Nushan and Daoxian xenoliths are associated with deep translithospheric faults (TLFZ). The mantle beneath the TLFZ is dominantly Phanerozoic in character (Zheng et al. 1998; Xu et al. 1998) and represents newly accreted materials that replaced the older lithosphere through extension, thermal erosion and melt-related metasomatism along the TLFZ (Zheng et al. 2004; Fan et al. 2000). Hebi is located near the Gravity Gradient Zone in eastern China, but away from any active fault. The mantle beneath this area escaped such replacement and represents a shallow relic of Archean lithosphere (Zheng et al. 2001).

Analytical methods

Major element analyses of minerals were carried out at Macquarie University using a Cameca SX50 electron microprobe (EMP), fitted with five crystal spectrometers, using an accelerating voltage of 15 kV and a sample current of 20 nA. The width of the electron beam was 5 μm. Standards were natural minerals, and matrix corrections were done after the method of Pouchou and Pichoir (1984). Counting times were 10 s for peaks and 5 s for background on either side of the peak. Major element abundances of rock-forming minerals reported in Table 1 generally represent averages of more than 5-point analyses of each grain and several grains from different parts of each sample. In order to examine whether equilibrium had been attained, considerable attention was paid to determine the homogeneity of individual phases. All of the minerals from Tuoyun peridotites are homogeneous.

Trace element analyses of minerals were carried out at Macquarie University using a 266 nm UV laser ablation microprobe coupled to an ICPMS (LAM-ICPMS). The laser ablation system is similar to the one described by Norman et al. (1996). The laser is a Continuum Surelite I-20 Q-switched and frequency quadrupled Nd:YAG laser with a fundamental infrared (IR) wavelength at 1,064 nm, quadrupled to 266 nm and a pulse width of 5–7 ns. Most analyses are done with beam energy in the range of 0.5–3 mJ per pulse. The ICPMS is a Hewlett-Packard HP 7500. The NIST 610 and 612 glasses were used as external standards; internal standards were Ca for clinopyroxene and amphibole and Mg for olivine, orthopyroxene and phlogopite. Data were reduced using the in-house GLITTER on-line software. Trace element abundances of olivine (Table 2), orthopyroxene (Table 3), clinopyroxene, amphibole and phlogopite (Table 4) represent averages of five points of analysis for each phase. Detection limits ranged from < 2 ppm for Ni to < 50 ppb for a variety of elements, including rare earth elements (REE), Nb, Th and U. Replicate analytical precision is 2–5%, with counting

Table 1 Electron microprobe analyses (wt%) of minerals from the Tuoyun peridotite xenoliths

Sample	T1c				T1e				T4p1				T2			T14d			T39bp2			T3bp2	
Rock	Sp lherzolite				Sp lherzolite				Sp lherzolite				Lherzolite			Lherzolite			lherzolite			Sp lherzolite	
Mineral	Cpx	Opx	Ol	Sp	Cpx	Opx	Ol	Sp	Cpx	Opx	Ol	Sp	Cpx	Opx	Ol	Cpx	Opx	Ol	Cpx	Opx	Ol	Cpx	Opx
Points	5	5	5	4	5	5	6	5	5	5	5	5	5	5	5	5	5	5	5	5	8	5	5
SiO_2	51.7	54.5	40.4	0.1	52.6	55.9	40.7	0.1	52.2	54.5	40.7	0.1	52.3	54.9	39.9	52.2	54.9	40.5	52.3	55.2	40.8	52.3	55.0
TiO_2	0.11	0.05	0.01	0.07	0.22	0.04	0.01	0.11	0.35	0.07	0.01	0.11	0.10	0.04	0.01	0.11	0.03	0.00	0.11	0.05	0.01	0.51	0.07
Al_2O_3	4.55	3.98	0.01	50.6	4.36	3.73	0.02	47.1	5.78	3.98	0.01	48.6	5.49	4.26	0.02	5.06	4.09	0.01	4.98	4.09	0.02	6.38	4.26
Cr_2O_3	0.70	0.46	0.03	15.6	1.21	0.50	0.03	19.6	1.26	0.48	0.01	19.2	0.86	0.49	0.03	0.79	0.48	0.02	0.79	0.49	0.02	0.61	0.34
FeO	2.84	6.03	9.54	11.5	2.70	6.28	10.2	11.9	2.62	5.94	9.25	11.4	2.83	6.26	9.85	2.74	5.91	9.38	2.83	6.01	9.50	2.94	6.52
MnO	0.08	0.14	0.19	0.00	0.07	0.12	0.13	0.00	0.10	0.14	0.15	0.00	0.08	0.13	0.12	0.09	0.13	0.14	0.04	0.16	0.15	0.06	0.11
MgO	16.6	33.1	49.5	19.9	16.0	32.8	48.7	18.9	15.5	33.3	50.2	19.2	15.8	33.1	49.8	16.1	33.3	50.1	16.5	33.1	49.5	15.1	32.9
CaO	21.5	0.90	0.06	0.01	21.6	0.76	0.06	0.05	19.7	0.86	0.06	0.01	20.5	0.88	0.07	20.8	0.90	0.12	21.1	0.84	0.09	19.9	0.78
Na_2O	0.77	0.05	0.01	0.00	0.95	0.14	0.00	0.00	1.85	0.05	0.01	0.02	1.39	0.12	0.00	1.41	0.12	0.00	1.03	0.08	0.01	1.91	0.13
K_2O	0.00	0.01	0.00	0.01	0.01	0.01	0.01	0.00	0.01	0.00	0.01	0.00	0.01	0.00	0.01	0.00	0.01	0.01	0.00	0.01	0.01	0.00	0.00
NiO	0.04	0.14	0.43	0.40	0.04	0.11	0.42	0.30	0.09	0.08	0.40	0.33	0.08	0.10	0.39	0.04	0.10	0.41	0.07	0.08	0.33	0.05	0.13
Total	98.8	99.3	100.2	98.2	99.7	100.4	100.3	98.0	99.5	99.3	100.7	98.9	99.4	100.3	100.2	99.3	100.0	100.7	99.7	100.2	100.4	99.7	100.2
$Mg^{\#}$	91.3	90.7	90.2	75.5	91.3	90.3	89.4	73.8	91.3	90.9	90.6	75.0	90.9	90.4	90.0	91.3	90.9	90.5	91.2	90.8	90.3	90.2	90.0
$Cr^{\#}$	9.2			17.1	15.8			21.9	12.7			20.9	9.6			9.5			9.7			5.9	
Mg/Fe																							

Sample	T24(b)							T24(a)				T4p2					T30					T3bp1	
Rock	Lherzolite							Amp peridotite (vein)				Sp lherzolite					Lherzolite					Sp dunite	
Mineral	Ol	Sp	Amp	Cpx	Opx	Ol	Amp	Cpx	Opx	OI	Amp	Cpx	Opx	Ol	Sp	Phl	Cpx	Opx	Ol	Bi		Ol	Sp
Points	5	5	5	5	5	5	5	5	5	5	5	5	5	5	5	5	5	8	5	3		5	5
SiO_2	40.7	0.0	42.3	52.5	55.4	40.1	42.9	52.9	55.6	39.9	42.9	52.2	54.8	39.9	0.1	37.3	53.3	54.7	39.8	34.2		38.5	0.2
TiO_2	0.01	0.10	2.00	0.08	0.01	0.01	0.51	0.13	0.04	0.00	0.55	0.34	0.09	0.01	0.12	3.51	0.18	0.05	0.01	6.74		0.03	1.10
Al_2O_3	0.01	55.6	14.4	6.12	4.31	0.02	15.4	4.18	4.22	0.01	15.4	5.70	3.73	0.02	47.3	17.2	2.23	3.54	0.01	14.4		0.06	53.8
Cr_2O_3	0.01	10.7	1.08	0.90	0.36	0.01	1.37	1.01	0.38	0.01	1.01	1.09	0.51	0.03	20.6	1.56	1.12	0.46	0.02	0.00		0.02	0.40
FeO	10.2	10.5	3.96	3.29	6.83	10.8	4.27	3.44	6.73	10.7	4.36	2.55	5.65	9.12	11.4	4.02	3.59	8.96	14.9	20.9		21.6	26.1
MnO	0.18	0.00	0.05	0.12	0.15	0.17	0.04	0.15	0.21	0.20	0.07	0.07	0.15	0.14	0.00	0.02	0.17	0.24	0.27	0.29		0.29	0.15
MgO	49.1	20.8	16.9	15.5	32.9	48.9	17.3	16.0	32.8	48.9	17.4	15.5	33.7	50.2	19.1	20.7	16.4	30.9	45.0	9.12		40.1	16.5
CaO	0.07	0.01	10.5	18.9	0.86	0.06	10.3	20.6	0.87	0.07	10.2	19.8	0.77	0.06	0.01	0.00	22.3	0.82	0.07	0.01		0.18	0.01
Na_2O	0.01	0.01	3.41	2.08	0.15	0.02	3.33	1.36	0.19	0.01	3.33	1.82	0.16	0.01	0.01	0.86	0.64	0.18	0.00	0.69		0.01	0.01
K_2O	0.01	0.00	1.19	0.01	0.01	0.00	1.45	0.03	0.01	0.01	1.48	0.00	0.01	0.00	0.00	8.83	0.04	0.00	0.00	8.71		0.00	0.01
NiO	0.34	0.33	0.14	0.02	0.08	0.35	0.16	0.04	0.09	0.33	0.05	0.04	0.13	0.38	0.29	0.15	0.05	0.10	0.29	0.09		0.13	0.20
Total	100.6	98.1	95.9	99.5	101.1	100.4	97.0	99.8	101.2	100.1	96.8	99.1	99.7	99.9	98.8	94.1	100.0	100.0	100.4	95.1		100.8	98.4
$Mg^{\#}$	89.6	77.8	88.4	89.4	89.6	89.0	87.8	89.2	89.7	89.1	87.6	91.5	91.4	90.8	75.0	90.2	89.0	86.0	84.4	43.8		76.8	52.9
$Cr^{\#}$		11.4		9.0				13.9				11.2			22.6		25.0						0.5
Mg/Fe																9.17				0.78			

statistics and the uncertainties on the determination of the internal standard concentrations accounting for most of the analytical uncertainty on an individual analysis. Additional descriptions for instrument operating conditions, calibration values, detection limits and error analysis for the laser microprobe are given by Norman et al. (1996).

Results

Sample description

Peridotite xenoliths are angular and small (3–3.5 cm across). Classification of the ultramafic xenoliths is based on the IUGS scheme (Le Maitre 1982), with some modification. Lherzolites are subdivided into Cpx-poor lherzolite, lherzolite and Cpx-rich lherzolite, based on Cpx/Opx of $<1/3$, 1/3–2/3 and $>2/3$, respectively (Zheng et al. 1998). The modal compositions of the xenoliths have been determined by point-counting 800–1,000 points in each thin section (Table 5) and show that Cpx-rich lherzolites (average Cpx/Opx = 0.74) are relatively abundant. Two amphibole-bearing lherzolites [T3bp2, T24(b)] and two mica-bearing (T4p2 and T30) peridotites were collected. Amphibole and mica occur in microcracks or along the boundaries of olivine and pyroxenes (Fig. 2a). All xenoliths except T3bp1 belong to the Cr-diopside suite of Wilshire and Shervais (1975) or Type I of Frey and Prinz (1978). T3bp1, containing olivine with low $Mg^{\#}$ (76.8) and spinel with low $Cr^{\#}$ (1.0), is regarded as an Al-augite suite or Type II xenolith. A composite xenolith (T24) contains an amphibole-rich lherzolitic vein [T24(a)]. All of these

Table 2 Trace element concentrations of olivine (ppm) in the Tuoyun peridotite xenoliths

Type	Volatile-free peridotite					Volatile-bearing peridotite				Hebi ($n=9$)[a] Average (range)	TLFZ ($n=9$)[a] Average (range)
Sample Points	T1c 5	T1e 5	T4p1 5	T14d 5	T39bp2 5	T3bp2 5	T24(b) 5	T4p2 5	T30 5		
Ca	1,444	997	852	1,829	905	1,669	980	986	1,288	1,034 (806–1,284)	546 (381–957)
Sc	3.87	3.43	3.59	3.97	3.77	4.07	3.29	3.52	3.39	4.18 (3.45–4.58)	3.29 (2.60–4.80)
Ti	8.80	10.3	10.9	7.73	6.92	14.6	4.59	13.6	8.70	12.8 (2.60–26.4)	16.6 (13.0–20.2)
V	2.15	2.35	2.37	3.12	2.61	2.30	2.10	2.18	1.96	2.74 (1.61–3.61)	2.09 (1.78–2.83)
Cr	74.2	85.3	67.9	84.8	74.4	55.0	68.9	83.7	83.9	176 (91.6–254)	47.5 (32.2–78.8)
Mn	875	940	872	895	869	964	1,018	817	1,670	788 (724–915)	913 (771–1,001)
Co	123	123	116	118	117	122	114	114	117	114 (107–122)	110 (94–127)
Ni	2,765	2,487	2,274	2,590	2,390	2,336	2,026	2,299	1,984	2,523 (2,300–2,725)	2,286 (1,998–2,601)
Zn	44.7	53.4	38.4	43.2	43.1	44.8	58.2	40.8	112	43.1 (37.4–58.7)	35.6 (26.2–50.8)
Ga	0.42	0.27	0.20	0.36	0.17	0.52	0.23	0.27	0.36	0.27 (0.15–0.38)	0.11 (0.06–0.18)
Ni/Cr	37.24	29.16	33.52	30.53	32.14	42.43	29.41	27.48	23.66	14.34 (10.73–25.27)	20.7 (19.8–21.3)
Ni/Co	22.56	20.17	19.58	21.92	20.39	19.18	17.75	20.21	17.01	22.13 (21.50–22.34)	52.1 (44.0–78.3)

[a]Author's unpublished data

peridotite xenoliths except T3bp1 and T24(a) show fine-grained microstructure (Fig. 2b), based on the classification of Harte (1977). The grain size of olivine and both pyroxenes is generally <2 mm. The grain size in T3bp1 and in the amphibole-rich vein [T24(a)] of the composite xenolith T24 reaches 3–4 mm, a medium-grained microstructure. In this paper, the amphibole/mica-bearing or -free xenoliths are referred to as "volatile-bearing" or "volatile-free" peridotites, respectively.

Mineral chemistry

Olivine

Olivine in the volatile-free peridotites except T1e has higher $Mg^{\#}$ (90.2–90.6) than those in the amphibole-bearing xenoliths (89.0–89.6). The $Mg^{\#}$ in T1e (89.4) is similar to those in amphibole-bearing xenoliths. $Mg^{\#}$ in the vein [T24(a)] and the host [T24(b)] of the composite xenolith are also similar. The highest $Mg^{\#}$ is found in a phlogopite-bearing peridotite (T4p2) and the lowest in biotite-bearing xenolith T30.

The olivine of the Tuoyun peridotites shows large ranges in Ca (852–1,829 ppm) and Ga (0.17–0.52 ppm), but limited variation in other trace element contents (Ni, Sc, Co, V, Mn and Zn), Ni/Cr and Ni/Co (Table 2). Sc and V contents generally are higher in olivine of the volatile-free peridotites than the volatile-bearing ones, where these elements are mainly contained in amphibole and mica (see Table 4). The Ca and Ga contents of olivine in the volatile-bearing samples are generally at the low end of the compositional range defined by the volatile-free peridotites. High CaO in the olivine of spinel peridotites is related to high equilibration

Table 3 Trace element concentrations of orthopyroxene (ppm) in the Tunyun peridotite xenoliths

Type	Volatile-free peridotite			Volatile-bearing peridotite				Hebi ($n=9$)[a] Average (range)	TLFZ ($n=9$)[a] Average (range)
Sample Points	T1e 5	T4p1 5	T39p2 5	T3bp2 5	T4p2 5	T24b 5	T30 5		
Ca	4,707	4,811	4,995	4,612	4,926	5,679	5,144	6,113 (5,300–6,738)	4,330 (3,594–5,742)
Sc	12.0	15.9	16.8	14.3	13.8	12.4	12.3	15.7 (12.0–19.2)	16.4 (13.5–21.1)
Ti	306	333	182	619	442	110	296	163(7.64–468)	596 (441–786)
V	65.0	72.1	78.2	68.0	61.8	53.5	54.9	51.4 (41.9–57.9)	66.8 (58.4–85.7)
Cr	2,666	2,321	2,443	1,703	2,789	2,238	2,562	3,981 (2,420–4,510)	1,781 (1,333–2,044)
Mn	975	869	874	968	848	1,036	1,581	808 (761–920)	914 (826–1,076)
Co	51.0	47.4	48.8	49.4	47.2	47.4	47.3	47.3 (46.6–50.6)	45.3 (38.9–55.2)
Ni	651	588	630	607	597	531	530	658 (622–676)	580 (491–687)
Zn	34.8	24.7	27.2	28.8	26.8	38.3	69.4	26.8 (24.3–34.5)	23.7 (16.2–34.8)
Ga	2.30	2.01	2.10	2.52	2.23	5.19	3.51	1.89 (0.89–4.15)	2.37 (1.59–3.55)
Sr	0.44	0.01	0.04	0.36	0.13	0.29	0.17	0.58 (0.01–1.07)	0.10 (0.03–0.20)
Y	0.41	0.54	0.49	0.83	0.52	0.89	1.03	0.22 (0.05–0.55)	0.97 (0.67–1.18)
Zr	0.37	0.22	0.16	0.90	1.06	6.50	1.69	1.20 (0.20–3.71)	1.45 (0.61–2.05)
Ni/Cr	0.24	0.25	0.26	0.36	0.21	0.24	0.21	0.17 (0.15–0.26)	12.89 (12.00–14.00)
Ni/Co	12.77	12.40	12.92	12.28	12.66	11.22	11.22	14.00 (13.52–14.52)	0.33 (0.24–0.45)

[a]Author's unpublished data

Table 4 Trace element concentrations of clinopyroxene, amphibole and phlogopite (ppm) in the Tuoyun peridotite xenoliths

Type	Volatile-free peridotite					Volatile-bearing peridotite							
Sample	T1e	T4p1	T2	T14d	T39bp2	T3bp2	T24(b)	T24(a)	T4p2	T30	T24(b)	T24(a)	T4p2
Mineral	Cpx	Cpx	Cpx	Cpx	Cpx	Cpx	Cpx	Cpx	Cpx	Cpx	Amp	Amp	Phl
Points	5	5	5	5	5	5	5	5	5	5	5	5	5
Li	6.58	4.61	9.00	5.92	6.06	8.26	4.15	3.13	10.18	9.63	7.04	7.87	6.71
Sc	75.3	62.6	66.1	66.1	69.5	73.6	56.0	55.0	74.3	73.2	43.0	44.0	24,587
Ti	2,283	1,285	785	674	791	3,546	1,771	2,864	2,264	1,747	14,986	12,937	21,054
V	274	179	238	208	227	277	188	185	236	251	301	650	9,791
Cr	8,258	8,599	5,869	5,391	5,391	4,163	6,893	6,142	7,439	7,643	9,350	7,370	60.6
Co	21.0	16.1	21.8	19.4	20.4	17.6	13.7	14.3	16.3	21.8	31.6	45.7	1,455
Ni	334	249	357	305	331	261	198	193	248	274	611	850	n.a.
Zn	9.58	6.43	10.1	8.62	8.81	8.43	8.56	7.43	9.17	23.7	17.1	12.5	79.7
Ga	3.11	1.69	4.51	2.40	2.37	4.44	4.72	5.12	3.34	8.01	18.8	13.9	n.a.
Rb	b.d.	b.d.	15.0	8.35	1.08	4.87	1.06	1.26	6.39	11.5	8.48	4.31	201
Sr	448	16.0	157	62.2	55.0	137	122	122	202	258	383	271	0.12
Y	9.26	9.23	12.5	9.54	8.34	18.3	16.0	16.1	11.0	21.4	17.7	25.2	11.1
Zr	8.20	3.93	49.7	57.9	3.15	23.1	147	150	32.1	56.2	214	272	41.5
Nb	0.74	0.37	2.71	2.54	1.40	0.29	0.48	1.01	0.26	1.26	75.0	153	n.a.
Ba	b.d.	< 0.20	40.7	10.3	1.91	9.49	1.87	1.80	14.8	54.3	160	98.0	1,686
La	10.3	0.40	17.4	5.16	8.06	3.72	11.4	12.0	9.18	8.84	16.5	18.1	0.32
Ce	18.8	0.74	37.4	9.03	11.6	7.50	26.2	25.9	12.0	30.1	30.9	40.7	0.49
Pr	1.84	0.13	4.49	0.98	1.11	1.00	3.41	3.59	1.34	4.86	4.28	5.94	0.06
Nd	5.63	1.00	16.8	3.27	3.25	4.94	11.7	12.3	5.53	22.8	14.8	22.9	0.34
Sm	1.13	0.53	2.76	0.61	0.43	1.77	3.92	3.77	1.47	5.12	4.73	6.75	0.03
Eu	0.42	0.22	0.81	0.18	0.16	0.62	1.29	1.58	0.54	1.80	1.44	1.74	b.d.
Gd	1.35	1.00	2.34	0.91	0.64	2.54	3.66	3.57	1.66	4.70	4.25	6.36	b.d.
Tb	0.21	0.20	0.35	0.18	0.15	0.45	0.55	0.56	0.30	0.71	0.60	0.87	b.d.
Dy	1.59	1.65	2.35	1.52	1.30	3.36	3.40	3.41	2.13	4.34	3.58	5.42	0.09
Ho	0.34	0.35	0.48	0.36	0.33	0.72	0.65	0.63	0.41	0.86	0.68	0.99	b.d.
Er	0.98	1.09	1.38	1.11	1.07	2.14	1.65	1.73	1.21	2.23	1.70	2.51	0.02
Tm	0.14	0.17	0.20	0.17	0.16	0.31	0.25	0.24	0.17	0.31	0.25	0.33	b.d.
Yb	1.00	0.99	1.30	1.18	1.11	2.03	1.43	1.60	1.17	2.16	1.52	1.95	0.04
Lu	0.13	0.15	0.18	0.17	0.16	0.29	0.19	0.20	0.16	0.29	0.20	0.24	b.d.
Hf	0.29	0.22	0.30	0.49	0.12	0.86	6.12	5.55	0.94	1.31	8.28	9.04	0.25
Ta	0.09	b.d.	0.46	0.51	0.14	0.04	0.13	0.15	0.06	0.14	5.21	10.1	0.98
Pb	0.45	0.29	0.26	0.17	0.44	0.37	0.16	0.13	0.62	0.39	1.00	0.79	0.46
Th	0.68	0.11	1.51	1.00	1.23	0.36	1.06	1.07	2.15	0.17	1.51	1.51	0.39
U	0.16	0.06	0.25	0.18	0.29	0.11	0.21	0.14	0.50	0.05	0.27	0.31	0.59

b.d. below detection limit, *n.a.* no analysis

temperatures (O'Reilly et al. 1996). T30 has the lowest Ni, V contents, the lowest Ni/Cr and Ni/Co values and the highest Zn and Mn contents among the Tuoyun peridotites (Fig. 3).

Orthopyroxene

The $Mg^{\#}$ of orthopyroxene in the volatile-free lherzolites is high (90.3–90.9) compared to those in the amphibole-bearing xenoliths (89.6–90.0). The phlogopite-bearing peridotite T4p2 has the highest $Mg^{\#}$ value (91.4), while the biotite-bearing xenolith T30 has the lowest (86.0).

The Opx shows large ranges in Ti (110–619 ppm), Mn (848–1,581 ppm), Zn (25–69 ppm), Ga (2.01–5.19 ppm), Sr (0.01–0.36 ppm) and Zr (0.16–6.50 ppm), but the range of Ni, Sc, Co and V contents, Ni/Cr and Ni/Co is limited (Table 3). Opx in the volatile-free peridotites has low Y and Zr contents, but high V and Ni/Co compared to the volatile-bearing ones. T30 and T24(b) have high Ca, Cr, Zn, Ga, Y and Zr contents, but low V, Ni contents and low Ni/Cr and Ni/Co.

Clinopyroxene

$Mg^{\#}$, $Cr^{\#}$ and minor elements The clinopyroxene in volatile-free peridotites shows higher $Mg^{\#}$ than those in the amphibole-bearing xenoliths. The $Mg^{\#}$ is highest in the phlogopite-bearing peridotite (T4p2), while it is lowest in the biotite-bearing xenolith (T30), which has the highest $Cr^{\#}$ among these Cr-diopside suite xenoliths.

The contents of Na_2O and Al_2O_3 show large ranges (0.64–2.08 and 2.23–6.38 wt%, respectively). There is no obvious difference in these minor elements between the volatile-free and volatile-bearing peridotites, except the latter has a wider range. The volatile-bearing peridotites except T4p2 have high FeO relative to the volatile-free ones. T4p2 has the lowest FeO content.

Table 5 Microstructure and mode of Tuoyun peridotite xenoliths from Tianshan, NW China

Suite	Type	Sample	Rock	Microstructure	Mode (%)					
					Ol	Opx	Cpx	Sp	Amp	Mica
I	Volatile-free peridotite	T1c	Sp lherzolite	Fine	52.0	26.0	21.5	0.5		
		T1e	Sp lherzolite	Fine	55.5	23.0	21.0	0.5		
		T4p1	Sp lherzolite	Fine	60.0	21.0	18.0	1.0		
		T2	lherzolite	Fine	54.0	24.5	21.5			
		T14d	lherzolite	Fine	57.0	25.5	17.5			
		T39bp2	lherzolite	Fine	51.0	26.0	23.0			
	Volatile-bearing peridotite	T3bp2	Sp lherzolite	Fine	56.5	27.5	14.0	1.5	0.5	
		T24(b)	lherzolite	Fine	59.5	24.0	12.0		4.0	
		T24(a)[a]	lherzolite	Medium	50.5	16.0	19.5		14.0	
		T4p2	Sp lherzolite	Fine	61.0	23.5	11.5	2.0		2.0
		T30	lherzolite	Fine	50.0	27.4	22.5			0.1
II		T3bp1	Sp dunite	Medium	97.0			3.0		
ECAOB ($n=42$)			Sp-Gnt lherzolite	Porphyroclastic to fine (main porphyroclastic)	63.0 (53.0–77.5)[b]	23.2 (15.0–30.0)	11.8 (5.1–25.0)	2.1 (1.0–4.0)	Frequent	Frequent
Hebi ($n=32$)			Sp lherzolite	Coarse to porphyroclastic (main coarse)	71.8 (58.2–85.5)	26.8 (15.3–40.8)	3.1 (0.5–6.4)	1.2 (0.0–5.0)	One	One
TLFZ ($n=49$)			Sp-Gnt lherzolite	Fine to coarse (main porphyroclastic)	63.6 (38.0–82.3)	24.3 (6.8–38.2)	8.2 (3.4–19.5)	2.7 (0.6–5.5)	Few	Few

ECAOB East Central Asian fold belt including Great Xing'an Mountains in China (Zhang et al. 2000), Dariganga in China/Mongolia (Wiechert et al. 1997) and Tariat in Central Mongolia (Kopylova et al. 1995; Ionov et al. 1997; Ionov 2002), Vitim (Glaser et al. 1999; Litasov et al. 2000) and Sikhote-Alin (Ionov et al. 1995) in east Siberia; *Hebi* refractory mantle in the Archean North China block (Zheng et al. 2001); *TLFZ* translithospheric fault zone areas including Shanwang (Zheng et al. 1998) and Nushan (Xu et al. 1998) in the Tanlu fault within the North China block and Daoxian in the Ningyuan-Jianghua fault within the Cathaysia block (Zheng et al. 2004)
[a]Vein in T24(b)
[b]Average (range)

Trace elements The Tuoyun clinopyroxene, especially in the volatile-free samples, shows large variations in La contents (from 0.40 to 17.38 ppm). The chondrite-normalized REE patterns of clinopyroxene vary from LREE-depleted (T4p1), through concave-upward (T14d and T39bp2), to LREE-enriched [T1e, T4p2, T2, T24(b) and T24(a)]. T3bp2 and T30 have high HREE contents relative to the others and show flat and convex upward LREE patterns, respectively (Fig. 4).

The spidergrams (Fig. 5) show that all of the Tuoyun clinopyroxene have small to moderate negative anomalies in Nb and Ti. Most show a positive anomaly in Sr, and all except T30 and T4p1 show negative anomalies in Ba and Pb. In the composite xenolith, negative Nb and Ti anomalies in clinopyroxene correspond to positive anomalies in amphibole. The pattern for clinopyroxene in the vein is similar to that in the host in the composite xenolith.

Y and Nb contents are higher, while Ti and Zr contents are lower in the clinopyroxene of the volatile-free peridotites than in those of the volatile-bearing xenoliths. There are large variations in La/Yb and LREE contents in the volatile-free samples relative to the volatile-bearing peridotites. There are no obvious positive correlations between $Cr^{\#}$ and La/Yb or negative correlations between $Cr^{\#}$ and incompatible trace elements (Fig. 6) nor are there any positive correlations between La and other incompatible trace elements. The lack of such correlations suggests that two events, primary depletion and secondary enrichment, might have affected the mantle beneath the Tuoyun area.

Spinel

Spinel in the Tuoyun peridotite xenoliths has low contents of Cr_2O_3 (10.71–20.55 wt%) and NiO (0.14–0.40 wt%) and low $Cr^{\#}$ (0.11–0.23), compared to cratonic chromium spinels (e.g., $Cr^{\#}=0.40$–0.91; Griffin et al. 1998; Zheng 1999). The $Cr^{\#}$ of spinel and clinopyroxene is a sensitive indicator of the extent to which mantle peridotites have lost their basaltic components (Frey and Prinz 1978; Preß et al. 1986). The low $Cr^{\#}$ of spinel and low $Mg^{\#}$ of coexisting clinopyroxene in most Tuoyun samples indicate that most of the upper mantle beneath the region has been subjected to relatively low degrees of melt extraction. However, most of them (except T3bp2, an amphibole peridotite) are at the higher end of the compositional range defined by samples from the TLFZ (Fig. 7), implying higher degrees of melt extraction. Average degrees of melting, calculated from spinel $Cr^{\#}$ (Hellebrand et al. 2001), are 7.0% for the Tuoyun xenoliths, compared to 4.2% for xenoliths from the TLFZ.

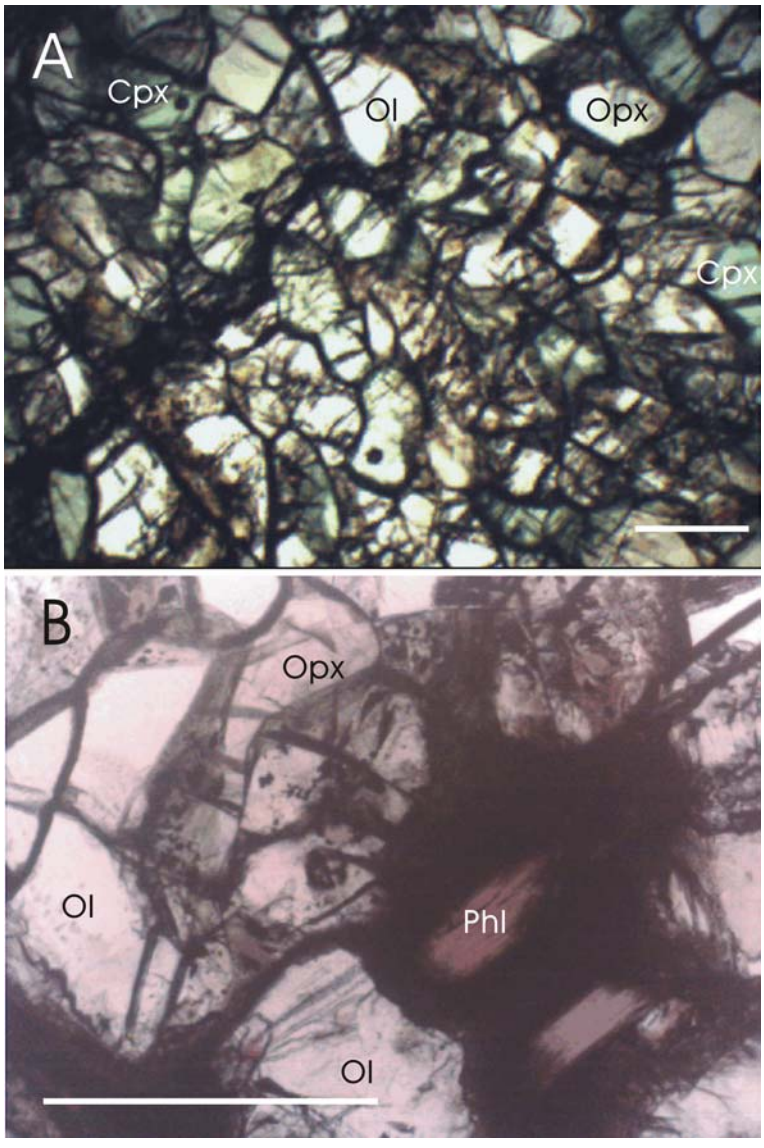

Fig. 2 Petrography of the Tuoyun peridotite xenoliths: **a** mica with black reaction rim along the boundaries of olivine and pyroxene; **b** fine-grained microstructure. *Scale bar*: 2 mm

Amphibole and mica

Amphiboles in T3bp2 and both in the vein and the host peridotite of the composite xenolith (T24) are classified as pargasite. However, amphibole in T3bp2 has a high content of TiO_2 (up to 2.00 wt%), while those in the composite xenolith have low TiO_2 contents (0.51–0.55 wt%). The amphiboles in the composite xenolith have high contents of Zr, Hf, Nb and Ta relative to the coexisting clinopyroxene. They show positive Nb, Ta and Ti anomalies in the spidergram, in contrast to the negative anomalies in the associated clinopyroxene. The incompatible element pattern for amphibole in the vein is similar to that in the host (see Fig. 5b).

Micas in T4p2 and T30 have Mg/Fe of 9.17 and 0.78 and are classified as phlogopite and biotite, respectively. Phlogopite in T4p2 ($Mg^{\#} = 0.90$) has 3.51 wt% TiO_2, 17.22 wt% Al_2O_3 and 1.56 wt% Cr_2O_3, while biotite in T30 ($Mg^{\#} = 0.44$) has 6.74 wt% TiO_2, 14.37 wt% Al_2O_3 and 0.29 wt% MnO. Phlogopite in T4p2 has much higher contents of Ti, Sc, V, Co, Zn, Ba and Rb, but much lower REE contents than the coexisting clinopyroxene.

Whole-rock composition (Table 6)

Compositions of the Tuoyun peridotites were reconstructed using their modes (Table 5) and mineral chemistry (Table 1), because the small sample sizes did not allow bulk analysis. The reconstructed compositions show that most of the Tuoyun peridotites are moderately refractory, with Al_2O_3 contents lower than the commonly accepted primitive upper mantle (PUM) compositions (e.g., Hart and Zindler 1986; McDonough and Sun 1995). However, most of these peridotites, including all of the volatile-free ones, are markedly high in CaO relative to Al_2O_3 (CaO/Al_2O_3 of 1.5–3.5, except T3bp2 and T4p2 with Ca/Al of 0.9–1.0) and plot above the Oceanic Trend (Boyd 1997; Fig. 8). This reflects the high clinopyroxene modes of the samples (see Table 5).

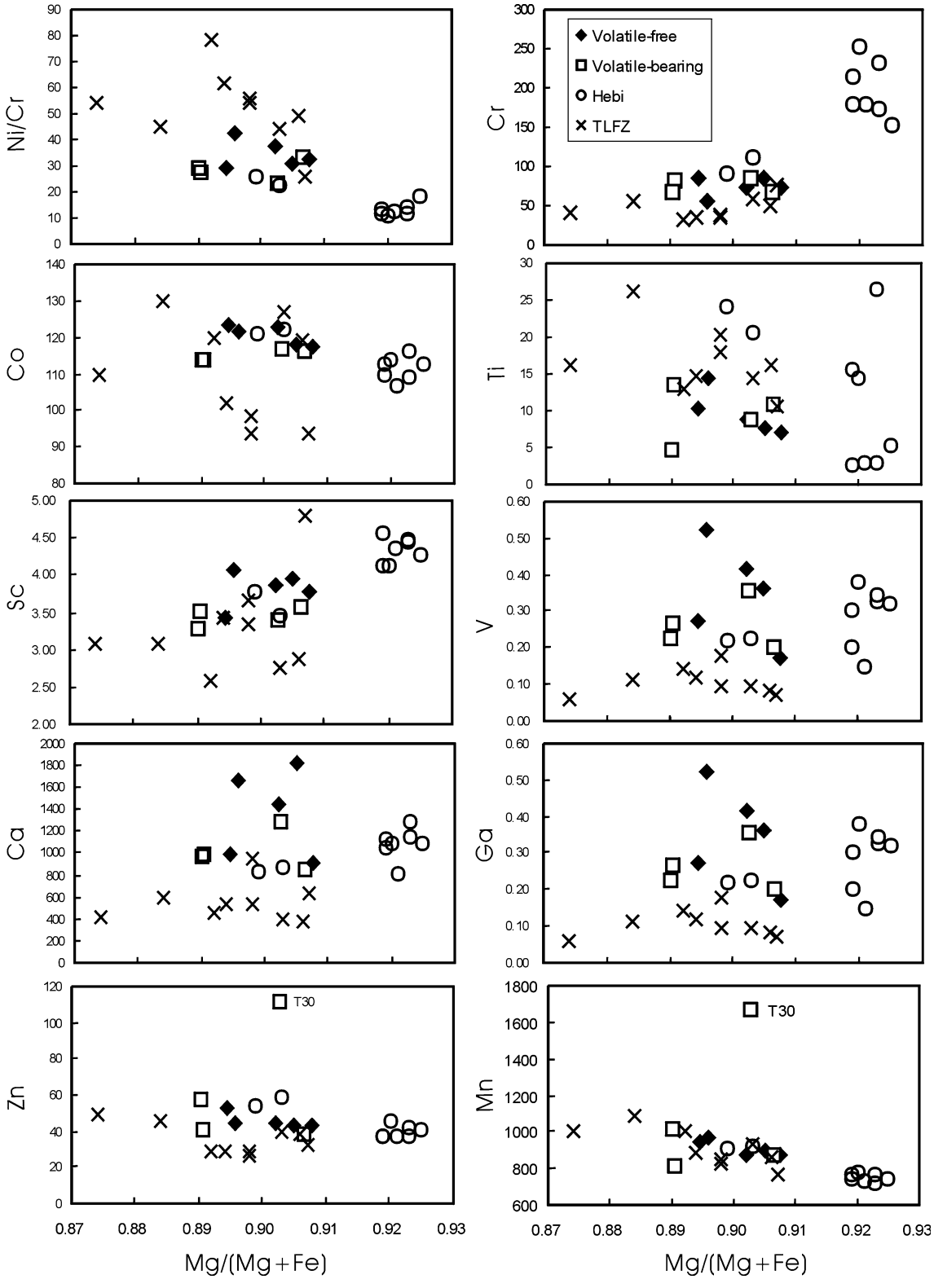

Fig. 3 $Mg^{\#}$ versus Ni/Cr and trace element contents (in ppm) in olivine from Chinese peridotites. Data sources for Hebi: Zheng et al. (2001) and TLFZ: Zheng et al. (1998, 2004)

Major elements do not show any correlations with MgO, except for negative correlations between MgO and CaO (Fig. 9). All the Tuoyun peridotites have low contents of FeO, TiO_2 and Al_2O_3, except for the three volatile-bearing peridotites [T30, T3bp2 and T24(b)], which have high contents of FeO relative to the PUM.

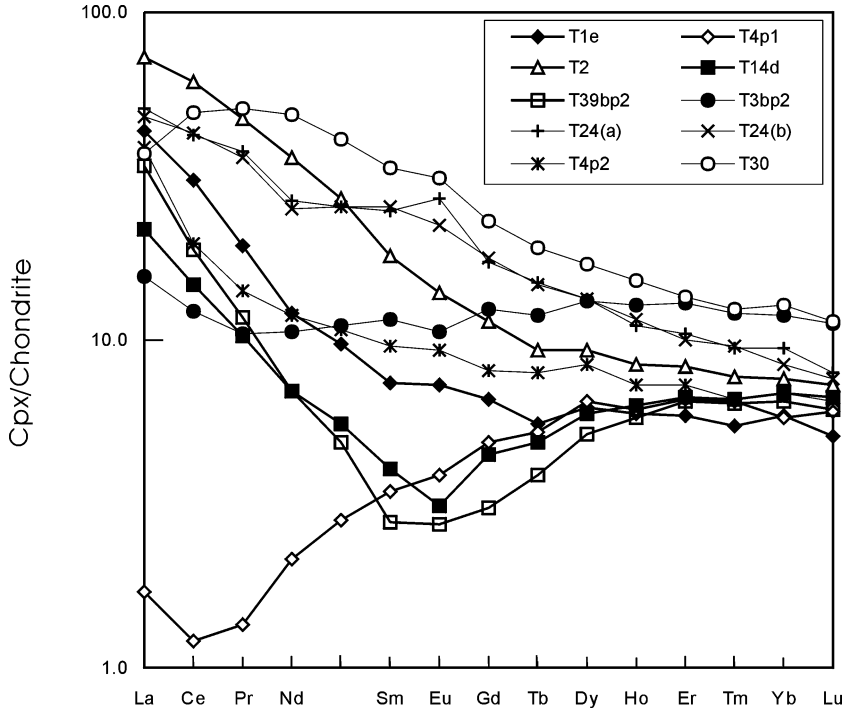

Fig. 4 REE patterns of Tuoyun mantle clinopyroxenes

T4p2 (a phlogopite-bearing peridotite) has high MgO but low TiO_2 and Al_2O_3 contents, within the compositional range defined by the Hebi peridotites. However, it has lower $Mg^{\#}$ than the latter due to its high FeO content.

Equilibration temperatures

Equilibration temperatures (T) for the Tuoyun peridotites have been estimated using several published thermometers, based on Fe–Mg partitioning between pyroxenes (Wells 1977; Sachtleben and Seck 1981), Ca content in orthopyroxene (Brey and Kohler 1990a, b) and Al exchange between olivine, orthopyroxene and spinel (Witt-Eickschen and Seck 1991). The three thermometers give similar temperature estimates (Table 7). Estimates based on the Brey and Kohler (1990b) Ca in Opx thermometer fall within the range of 894–1,060°C. Equilibration pressure cannot be estimated for the Tuoyun spinel peridotite xenoliths and no xenolith-based geotherm can be constructed. However, if we assume that the Tuoyun xenoliths represent the uppermost part of the SCLM with a maximum depth of 58 km, their equilibration temperatures are similar to those inferred from the advective geotherms at the same depth for Nushan (Xu et al. 1998) and Tariat (Ionov et al. 1998), two basaltic provinces associated with rifting.

Discussion

Extraction of basaltic melts

$Cr^{\#}$ values of coexisting spinel and clinopyroxene are sensitive indicators of the extent to which mantle spinel peridotites have lost their basaltic components (e.g., Frey and Prinz 1978; Preß et al. 1986). Most of the Tuoyun clinopyroxene and spinel have $Cr^{\#}$ values in the high end of the range defined by the mineral phases in xenoliths from the TLFZ (Fig. 7). This indicates that a relatively large volume of the upper SCLM has been subjected to melt extraction in these samples. Broad negative correlations between $Cr^{\#}$ and moderately incompatible elements (e.g., Y, Ti) and broad positive correlation between $Cr^{\#}$ and La/Yb in the clinopyroxene (except T30, Fig. 6) suggest that these elements behaved similarly in the upper SCLM over a wide region during partial melting and, therefore, can be used to model partial melting degree of the xenoliths (Jonson et al. 1990; Norman 1998).

Modeling using Y and Yb contents in the Cpx and assuming $K_d^{Y} = 0.42$ and $K_d^{Yb} = 0.40$ (Norman 1998) and the primitive mantle composition of Sun and McDonough (1989) indicates that the two least depleted samples are residues of less than 3% partial melting when either a batch or fractional melting model is adopted, whereas the others have experienced somewhat higher degrees of partial melting, i.e., 5–8% for fractional melting or 10–15% for batch melting (Fig. 10a), similar to the estimation based on the $Cr^{\#}$ of spinel (Hellebrand et al. 2001) mentioned above. The modeling assumes that these elements have only been modified by the partial melting event and that the partitioning of the elements between Cpx and melt is constant under upper mantle conditions. Modeling using Ti contents and assuming $K_d^{Ti} = 0.35$ (Norman 1998) requires even lower degrees for fractional melting (< 5%) and similar degrees for batch melting (Fig. 10b). The discrepancy may reflect a later introduction of Ti in the volatile-bearing to the

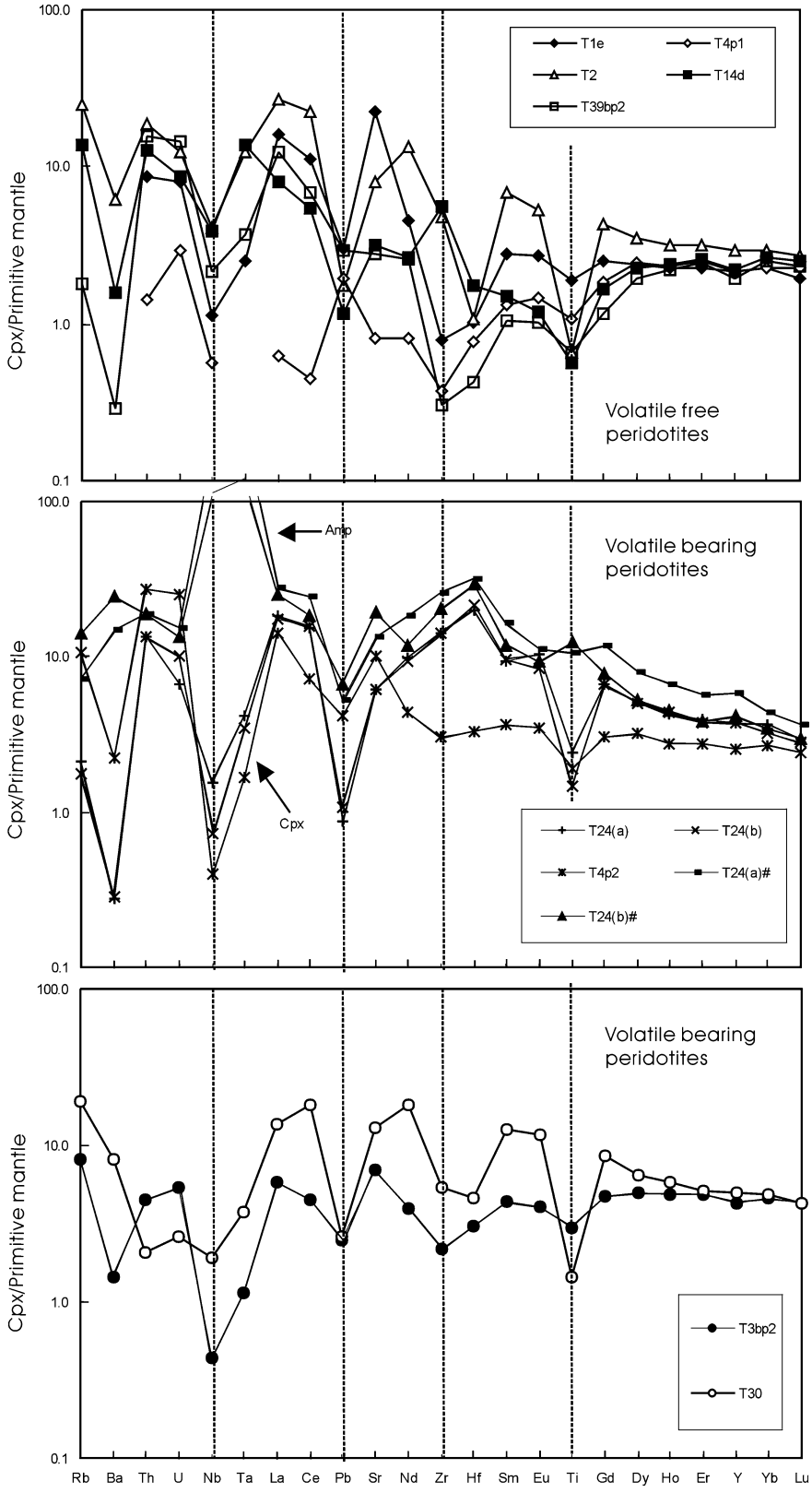

Fig. 5 Spidergrams of Tuoyun mantle clinopyroxenes and amphiboles: **a** "volatile-free" peridotites; **b**, **c** "volatile-bearing" peridotites

volatile-free peridotites (Fig. 9) during metasomatism in the continental setting (Norman 1998) as indicated by the presence of Ti-rich amphibole and phlogopite in the Tuoyun xenoliths. As Zr correlates with MREE and Sr, but not with Y, Yb or Ti, it is likely that Zr contents in the Tuoyun Cpx have also been modified during metasomatism.

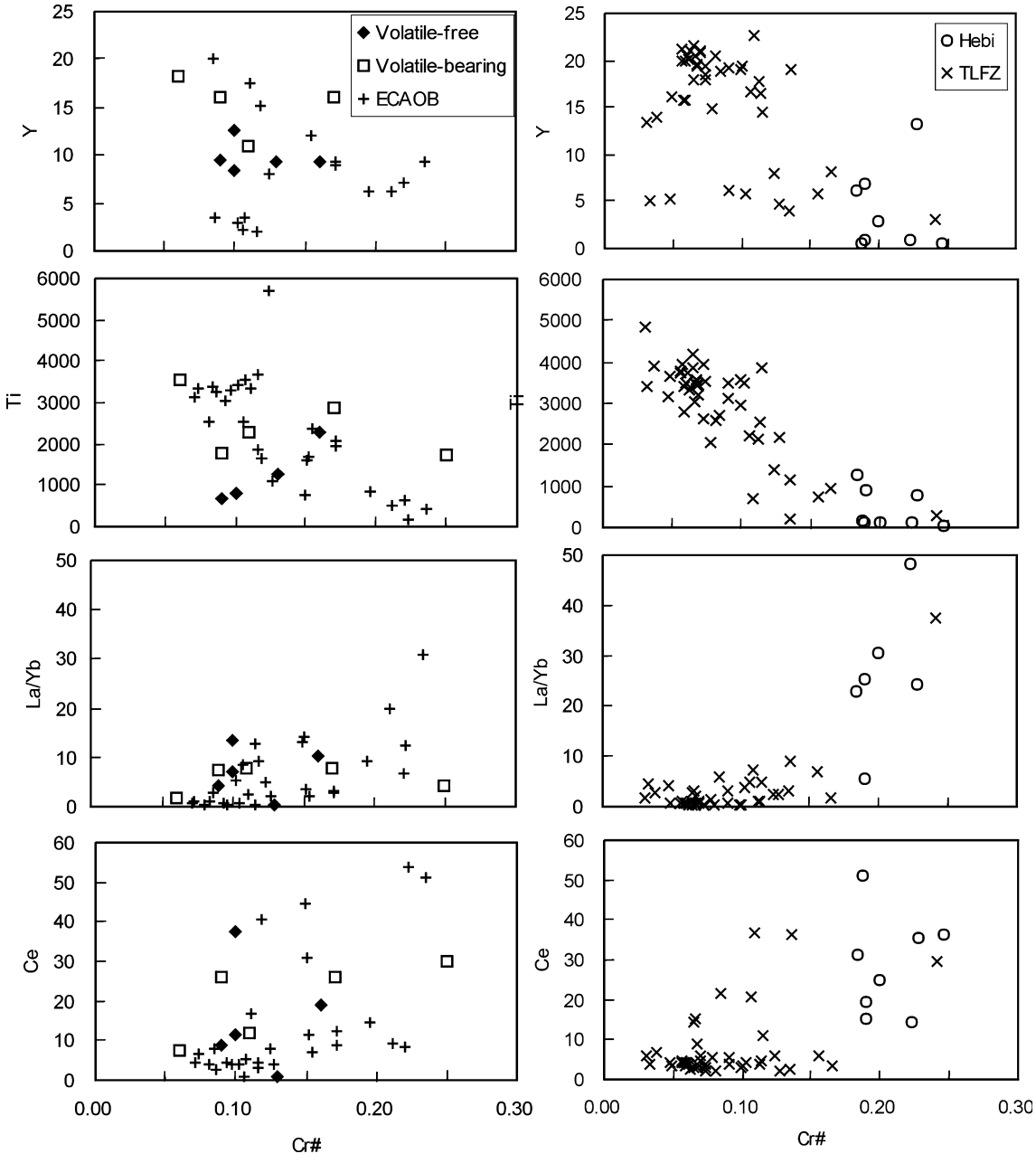

Fig. 6 $Cr^{\#}$ versus Y, Ti, La/Yb and Ce in Cpx from Chinese peridotites. Data sources for ECAOB: Wiechert et al. (1997), Ionov et al. (1995, 1997, 1998) and Glaser et al. (1999); Hebi: Zheng et al. (2001); TLFZ: Zheng et al. (1998, 2004) and Xu et al. (1998)

These models, combined with the low $Mg^{\#}$ of their olivines, suggest that the Tuoyun xenoliths are less refractory (Fig. 11a) than many of those in the ECAOB (8–13% melting; Ionov et al. 1995; Glaser et al. 1999; Zhang et al. 2000), and especially those from Hebi on Archean North China Craton (10–25% melting; Zheng et al. 2001). The ranges in olivine $Mg^{\#}$ and in the modeled degree of fractional melting for the TLFZ xenoliths are large. These xenoliths are commonly associated with different crustal terranes and tectonic settings and represent a mixture of older lithospheric mantle and mainly newly accreted material, which is slightly more fertile (< 5% fractional melting; Zheng et al. 1998, 2004; Xu et al. 2000) than the Tuoyun mantle in general. The difference can also be seen in the $Cr^{\#}$ of spinel (see above).

Mantle metasomatism

The majority of the Tuoyun spinel peridotites plot above the oceanic trend (Boyd 1997) on the Al_2O_3 versus CaO diagram (Fig. 8), suggesting strong secondary enrichment in Ca. High Mn, Zn and low $Mg^{\#}$ in T30 (Fo = 84), which contains 0.1% biotite, accompany enrichment in Fe. Other metasomatic signatures include: (1) the

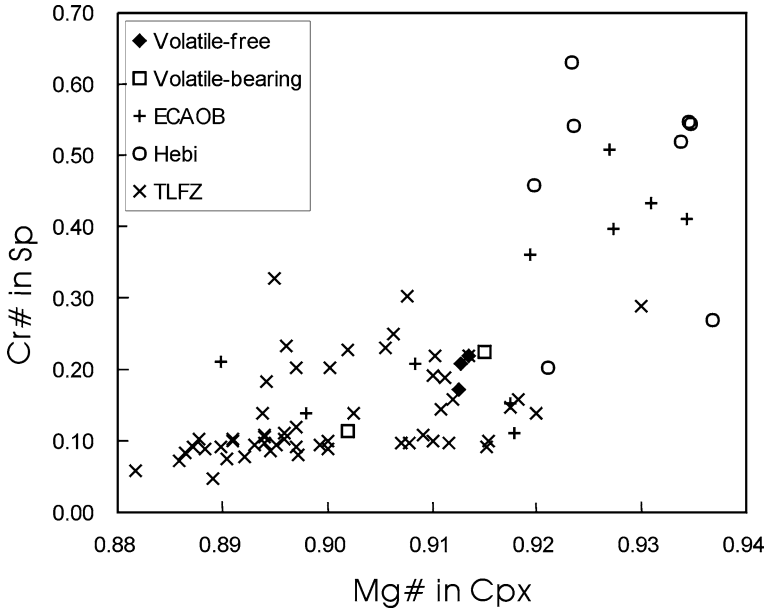

Fig. 7 $Mg^{\#}$ in Cpx versus $Cr^{\#}$ in Spinel from Chinese peridotite xenoliths. Data sources: as in Fig. 6

Table 6 Average (range) of reconstructed compositions for the Tuoyun peridotite xenoliths

Location	Tuoyun ($n=9$)	ECAOB ($n=18$)	Hebi ($n=32$)	TLFZ ($n=49$)
SiO_2	45.4 (41.5–47.2)	43.9 (40.6–45.9)	44.8 (39.0–47.6)	42.9 (38.4–46.0)
TiO_2	0.06 (0.04–0.12)	0.12 (0.05–0.23)	0.01 (0.00–0.04)	0.08 (0.00–0.20)
Al_2O_3	2.25 (1.37–2.98)	2.87 (0.42–5.27)	0.87 (0.38–1.69)	3.25 (0.72–5.00)
Cr_2O_3	0.39 (0.17–0.53)	0.35 (0.15–0.49)	0.58 (0.10–2.48)	0.67 (0.10–1.39)
FeO	7.07–9.55 (7.71)	8.16 (7.31–9.63)	6.87 (6.09–8.47)	8.83 (7.47–10.63)
MnO	0.13 (0.11–0.16)	0.19 (0.13–0.33)	0.11 (0.07–0.13)	0.14 (0.09–0.41)
MgO	39.5 (37.6–41.1)	41.4 (35.9–49.2)	46.1 (44.1–50.5)	41.8 (34.5–47.0)
CaO	3.94 (2.55–5.11)	2.48 (0.11–4.35)	0.49 (0.02–2.71)	1.90 (0.41–4.14)
Na_2O	0.29 (0.18–0.40)	0.22 (0.01–0.41)	0.05 (0.00–0.18)	0.16 (0.01–0.39)
K_2O	0.03 (0.00–0.14)	0.08 (0.00–0.40)	0.01 (0.00–0.02)	0.04 (0.00–0.12)
NiO	0.26 (0.21–0.30)	0.21 (0.09–0.30)	0.30 (0.24–0.39)	0.30 (0.16–0.36)
Total	100.0 (99.6–100.3)	99.8 (98.9–100.5)	100.2 (99.0–101.1)	99.9 (98.4–100.9)
$Mg^{\#}$	0.90 (0.89–0.91)	0.90 (0.89–0.90)	0.92 (0.91–0.93)	0.89 (0.87–0.91)
Mg/Si	1.18 (1.09–1.34)	1.42 (1.32–1.61)	1.47 (1.30–1.88)	1.42 (1.15–1.67)
FeO/MgO	0.20 (0.18 –0.22)	0.20 (0.20–0.21)	0.15 (0.14–0.18)	0.21 (0.19–0.25)
CaO + Al_2O_3	6.19 (4.10–7.33)	5.35 (0.53–9.63)	1.36 (0.40–3.94)	5.12 (1.13–7.93)

ECAOB East Central Asian fold belt (adapted from Ionov et al. 1993, 1997; Kopylova et al. 1995; Wiechert et al. 1997; Glaser et al. 1999; Litasov et al. 2000; Zhang et al. 2000; Ionov 2002); Hebi (adapted from Zheng et al. 2001); TLFZ (adapted from Qi et al. 1995; Zheng et al. 1998, 2004; Xu et al. 2000)

occurrence of amphibole and phlogopite, (2) the ubiquitous LREE- and MREE-enriched REE patterns in Cpx and (3) the high abundances of incompatible elements such as Th, Sr and LREE in Cpx. The transition from depleted Cpx REE patterns (T4p1) to concave-upward ones reflecting addition of LREE (T14d and T39bp2) in volatile-free lherzolites and finally to relatively steep negative trends (T1e and T2) (Fig. 4) is readily interpreted in terms of progressive metasomatism of originally depleted spinel peridotites.

Enrichment in large ion lithophile elements (LILE) and LREE has been attributed to metasomatism by carbonatitic melts (e.g., Meen 1987; Yaxley et al. 1998), volatile-rich silicate melts (Zangana et al. 1999; Zhang et al. 2000) or H_2O–CO_2 fluids (Ionov et al. 1995, 1997; Stalder et al. 1998). The experimental comparison of trace element partitioning between clinopyroxene and melt in carbonate and silicate systems shows that in the carbonate system clinopyroxene-melt partition coefficients for Si, Al, heavy REE, Ti and Zr are higher by factors of 5–200 than in the silicate system. Conversely, partition coefficients for Nb, LREE, alkali metals and alkaline earths show much less fractionation (<3; Blundy and Dalton 2000). On the other hand, relative to silicate melt or CO_2-rich fluid, carbonatite melts can fractionate REE and HFSE more effectively (Blusztajn and Shimizu 1994) and have high contents of LILE (Meen 1987), whereas Nb cannot be transported by H_2O-rich fluids (Eggler 1987). Therefore, the metasomatic agent reflected in the Tuoyun xenoliths is unlikely to be an H_2O-rich fluid. However, it is difficult to explain Zr enrichment with only carbonatitic metasomatism; the

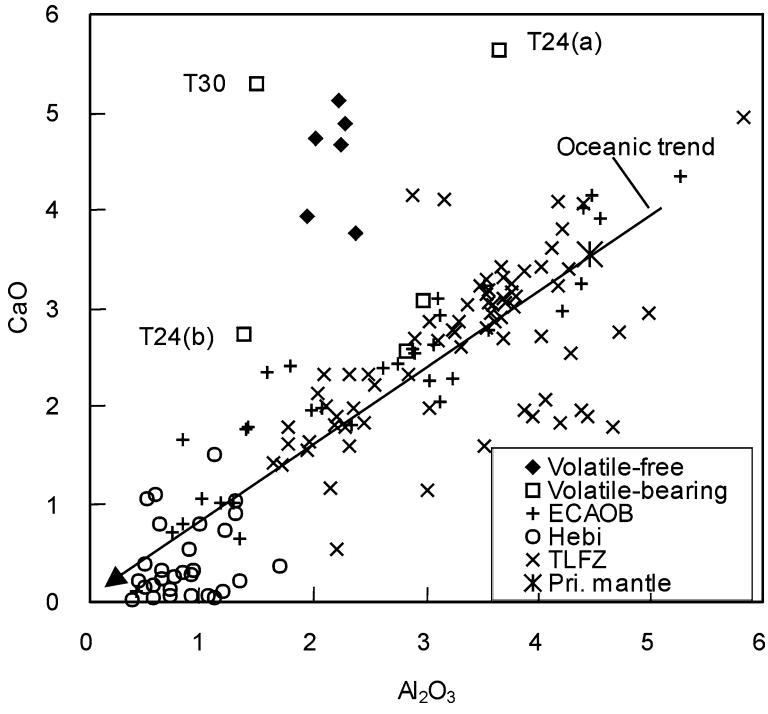

Fig. 8 Al_2O_3 versus CaO in Chinese peridotite xenoliths. Data sources: as in Fig. 6. Primitive mantle: McDonough and Sun (1995); Oceanic trend: Boyd (1989, 1997)

Zr enrichment seen in the clinopyroxene of the volatile-bearing to the volatile-free peridotites suggests the action of other Zr-rich melts. Thermodynamic calculations indicate that Ca-enrichment in spinel peridotites reflects their equilibration with SiO_2-undersaturated melts and can be produced by any SiO_2-undersaturated melts, either carbonatite melts or silicate melts (Zinngrebe and Foley 1995). This makes it difficult to constrain the nature of metasomatism agents.

High Ca/Al values, HFSE depletion and low Ti/Eu values in mantle clinopyroxenes have been widely interpreted as the key signatures of carbonatite-related metasomatism (e.g., Rudnick et al. 1993; Klemme et al. 1995; Coltorti et al. 1999). The most important metasomatic agents appear to have been silicate melts beneath the Cathaysia block and particularly beneath the TLFZ (Zheng et al. 1998, 2004), carbonatitic melts beneath the Archean mantle in Hebi (Zheng et al. 2001) and SiO_2-undersaturated potassic melts beneath the Wudalianchi area of ECAOB (Zhang et al. 2000). Tuoyun clinopyroxene has large ranges in Ti/Eu (971–5,765) and $(La/Yb)_n$ (0.19–6.33). Three volatile-bearing [T30, T24(b) and T24(a)] and one volatile-free (T2) peridotite have high Ce contents and La/Yb, but low Ti/Eu, suggesting carbonatitic metasomatism (Fig. 11b). However, T4p1 (a volatile-free peridotite) and T3bp2 (a volatile-bearing one) have high Ti/Eu, but low Ce and La/Yb, suggesting silicate metasomatism. Three volatile-free (T1e, T14d and T39bp2) peridotites and a volatile-bearing (T4p2) peridotite have transitional Ti/Eu, which may imply an agent transitional between carbonatitic and silicate metasomatism or overprinting by multiple episodes of metasomatism (Coltorti et al. 1999). The presence of phlogopite and whole-rock $CaO/Al_2O_3 > 1$ (Ca metasomatism) could also reflect silicic carbonatite melts (Neumann et al. 2002). Therefore, they are interpreted as the metasomatism of hydrous carbonatitic and potassic melt or the cumulative effects of mantle metasomatism by different agents (carbonatite and small-volume silicate melts) through time due to the presence of a mixture of older lithospheric mantle and mainly newly accreted material.

Comparison with lithospheric mantle in other parts of China

Peridotite xenoliths from Hebi, interpreted as representing a relict Archean mantle, are spinel harzburgite (Cpx-free) and Cpx-poor lherzolites with high modal Opx (average 27 vol.%) and are mainly coarse-grained; only one amphibole-bearing lherzolite was found (Zheng et al. 2001). Mantle xenolith suites along the TLFZ reflect upwelling of asthenospheric mantle into weak SCLM in Phanerozoic time (e.g., Xu et al. 1998; Chen et al. 2001). These suites contain a high percentage of Cpx-rich spinel lherzolites and high proportion of fine-grained and sheared microstructures (Zheng et al. 1998, 2004), some of which are ultra-fine-grained peridotitic/serpentinitic mylonites (Xu et al. 1996). Peridotite xenoliths in the ECAOB are porphyroclastic to fine-grained with mainly porphyroclastic microstructure and a wide variety in Cpx modes (5.1–25 vol.%, Preß et al. 1986; Stosch et al. 1986; Ionov et al. 1995, 1997; Kopylova et al. 1995; Wiechert et al. 1997; Glaser et al. 1999; Litasov et al. 2000; Zhang et al. 2000). Compared

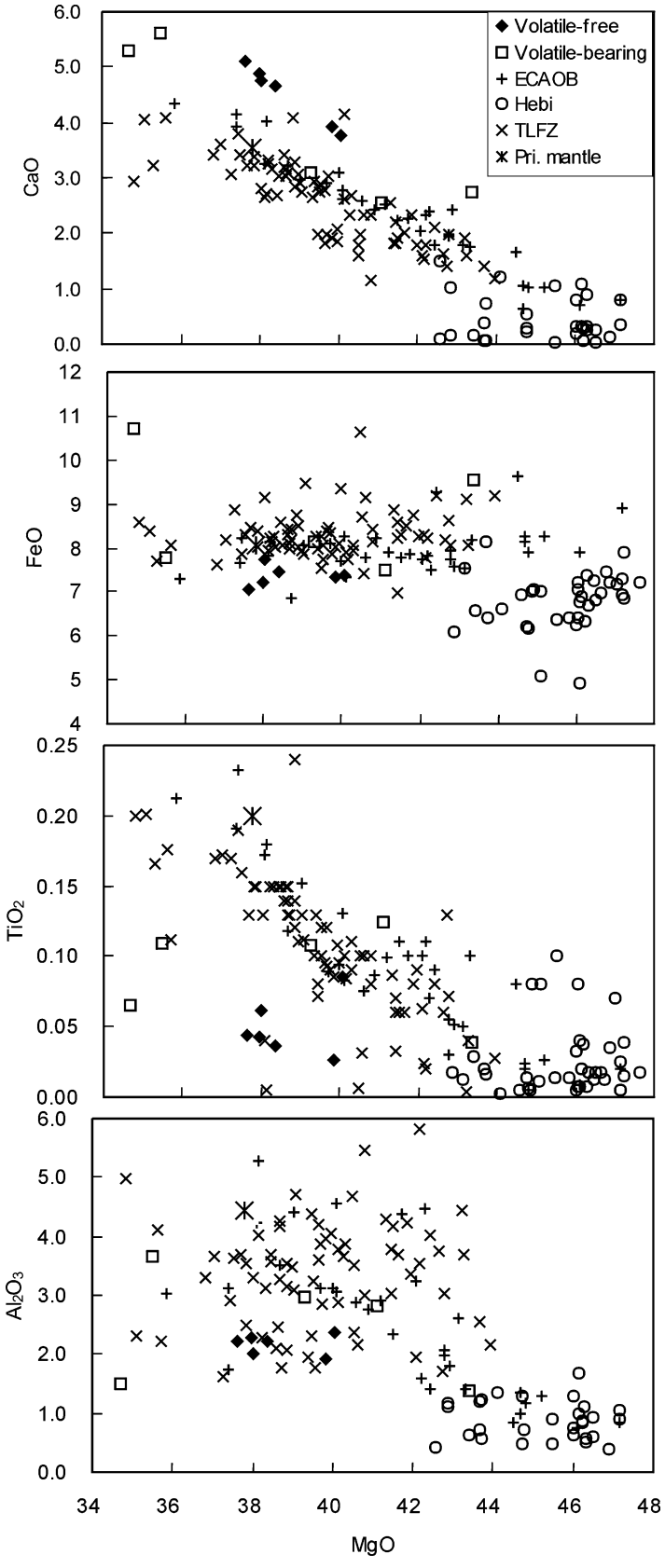

Fig. 9 MgO versus CaO, FeO, TiO_2 and Al_2O_3 in Chinese peridotite xenoliths. Data sources: as in Fig. 6. Primitive mantle: McDonough and Sun (1995)

to the above-mentioned localities, the Tuoyun peridotites are distinguished by a high proportion of fine-grained microstructures and a high proportion of amphibole/mica-bearing lherzolites, with high Cpx/Opx values.

Table 7 Temperature estimation for the Tuoyun peridotite from Tianshan (°C)

Suite	Sample	*T* (BK) Ca in Opx	*T* (Wells) Opx-Cpx	*T* (SS, a) Opx-Cpx	*T* (SS, b) Sp-Opx	*T* (SS, c) Sp-Opx	*T* (WEK, a) Sp-Opx	*T* (WEK, b) Cr-Al-Opx
Volatile-free peridotite	T1c	937	993	986	980	990	969	992
	T1e	951	952	976	979	991	977	990
	T2	1,012	985					
	T4p1	1,021	974	1,006	1,021	998	1,008	999
	T39bp2	1,013	1,002					
Volatile-bearing peridotite	T3bp2	995	1,002	979	935	953	928	953
	T4p2	1,015	969	982	1,003	997	987	999
	T14d	979	970					
	T24b	1,060	1,004					
	T30	894	932					

T (BK): Ca in Opx thermometer, Brey and Kohler (1990b); *T* (Wells): Wells (1977); *T* (SS, a), *T* (SS, b) and *T* (SS, c): two-pyroxene thermometer, Sp-Opx thermometer (Fe as Fe_{Total}) and Sp-Opx thermometer (Fe as Fe^{3+}), Sachtleben and Seck (1981) (Fe as Fe^{3+}), Sachtleben and Seck (1981); *T* (WEK, a) and *T* (WEK, b): Sp-Opx thermometer and Cr-Al-Opx thermometer, Witt-Eickschen and Seck (1991)

Mineral chemistry

The $Mg^{\#}$ and $Cr^{\#}$ of olivine and orthopyroxene in the Tuoyun peridotite xenoliths are mainly intermediate between those from Hebi and the TLFZ (see Figs. 3, 7). The most trace element contents (e.g., Ca, Ga, Cr and V) of olivine are high in the Tuoyun xenoliths relative to those in the TLFZ, whereas Ti contents and Ni/Cr value are lower, although the two areas have similar $Mg^{\#}$. The Cr contents of Tuoyun orthopyroxene are higher than those in the TLFZ, Y and Ti contents are low, especially in the volatile-free peridotites (see Table 3). The $Cr^{\#}$ of clinopyroxene and spinel in these samples are mainly at the higher end of compositional range defined by the TLFZ xenoliths (see Figs. 6, 7) and similar to the high-$Cr^{\#}$ group of the

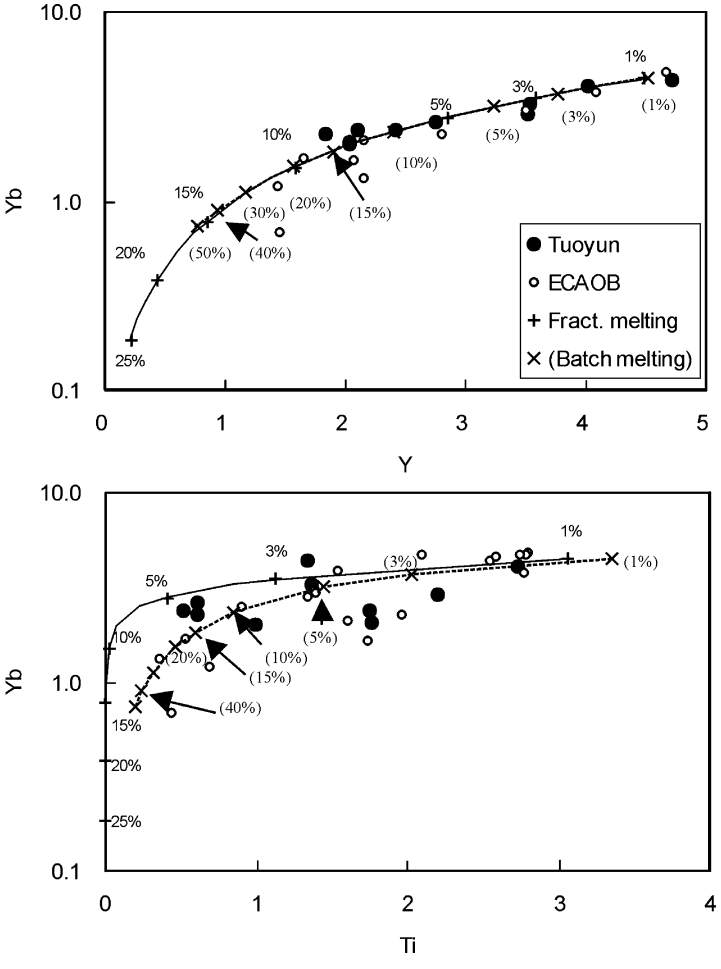

Fig. 10 Modeling of Cpx compositions using primitive mantle-normalized abundances. Adapted from Norman (1998). Fractional melting points are for 1, 3, 5, 10, 15, 20 and 25%; batch melting points are for 1, 3, 5, 10, 15, 20, 30, 40 and 50%

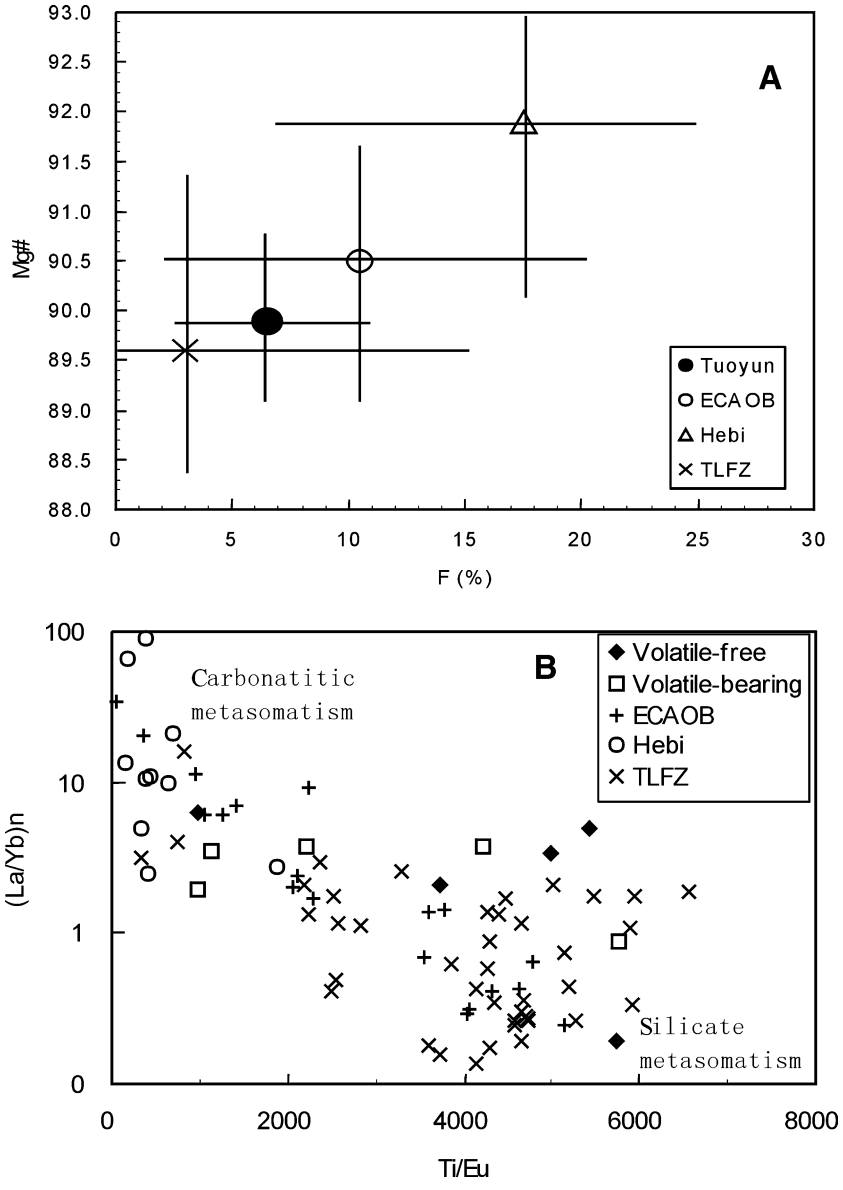

Fig. 11 **a** Degree of fractional melting (%) versus $Mg^{\#}$ in olivine; **b** Ti/Eu versus $(La/Yb)_n$ in clinopyroxene from Chinese peridotite xenoliths. **a** The *solid point* and *cross* represent the average and range for Tuoyun peridotites, respectively. **b** and silicate metasomatism, after Coltorti et al. (1999). Data sources: as in Fig. 6

WEK xenoliths in the ECAOB (Zhang et al. 2000). Cpx in T30 has high $Cr^{\#}$ (0.25), similar to values in Hebi Cpx (Zheng et al. 2001).

Ni/Cr ratio and the abundances of the compatible elements (e.g., Ni, Cr, Y and Sc) in olivine and orthopyroxene are lower than those from Hebi, but higher than those from the TLFZ. In contrast, the Mn, Ti and V contents of Tuoyun olivine and orthopyroxene are higher than those from Hebi, but lower than those from the TLFZ. Similarly, the average abundances of minor elements such as Na and Al and the moderately incompatible elements, such as Ti and Y, in Tuoyun clinopyroxenes are higher than those from Hebi, but lower than those from the TLFZ (see Fig. 6). In contrast, the La/Yb ratio and highly incompatible elements, such as LREE and Sr, in Tuoyun clinopyroxenes are lower than those from Hebi, while higher from those in the TLFZ (see Fig. 6).

Bulk rock composition

The low Al_2O_3, TiO_2, FeO contents and FeO/MgO ratio of the Tuoyun xenoliths, relative to the primitive mantle, suggest the extraction of basaltic melts (see Figs. 8, 9). However, most of the Tuoyun peridotite xenoliths have low MgO contents, but high CaO, Al_2O_3, TiO_2, FeO contents and high CaO/Al_2O_3 and FeO/MgO ratios, relative to the Hebi high refractory mantle (Zheng et al. 2001), implying only moderate degree of depletion. The Tuoyun peridotites are broadly similar in terms of the FeO/MgO and CaO + Al_2O_3 to the TLFZ mantle but are significantly enriched in CaO relative to Al_2O_3. These observations, coupled with the mineral chemistry described above, imply that the Tuoyun mantle is moderately refractory and intermediate in composition between the SCLM in the Hebi and TLFZ areas (see Tables 2, 3 and Fig. 3).

Comparison with the ECAOB peridotites

Detailed studies on peridotitic xenoliths (e.g., Preß et al. 1986; Stosch et al. 1986; Ionov et al. 1995, 1997; Kopylova et al. 1995; Wiechert et al. 1997; Glaser et al. 1999; Litasov et al. 2000; Zhang et al. 2000) suggest the partial preservation of a Proterozoic lithospheric mantle section within the Phanerozoic accreted materials in the Wudalianchi and Sikhote-Alin areas of the ECAOB. The Tuoyun mantle section is situated in the western part of the belt. Its xenoliths are similar in terms of the major and minor elements of clinopyroxene to those reported from the ECAOB (see Figs. 6, 7), and high proportions of volatile-bearing peridotites with similar whole-rock CaO + Al_2O_3 and FeO/MgO are common throughout the belt. However, the Tuoyun xenoliths are distinct from most other ECAOB xenolith suites in having: (1) higher Cpx/Opx (i.e., CaO enrichment; see Figs. 8, 9), (2) higher proportions of fine-grained microstructures (see Table 5) and (3) lower olivine $Mg^{\#}$ and slightly lower degrees of fractional melting (see Fig. 11a).

Tectonic implications

Lithospheric peridotites are represented by: (1) "cratonic" xenoliths carried in magmas (kimberlite and alkaline extrusives) that erupt through Archean cratons; (2) "off-craton" xenoliths carried in alkali basalts that erupted in Proterozoic and younger continental regions; and (3) "massif peridotites", which are tectonic fragments of upper mantle interleaved with crustal rocks in Phanerozoic fold belts. Their ranges of variation can be illustrated on plots of modal olivine content versus $Mg^{\#}$ (Fig. 12). The depleted peridotite xenoliths derived from the Cathaysia block may represent a minor Proterozoic component preserved within a mainly Phanerozoic mantle (Qi et al. 1995; Xu et al. 2000; Zheng et al. 2004). The Hebi peridotites are interpreted as relics of the Archean lithosphere preserved locally at relatively shallow levels in the western part of the eastern North China Craton (Zheng et al. 2001). The mantle beneath the Shandong Peninsula represents a mixture of Archean lithospheric mantle and newly accreted material (Zheng et al. 1998). Although majority of the Tuoyun xenoliths plot in the area of Phanerozoic lherzolites, a few show a trend toward typically Proterozoic SCLM compositions (Fig. 12).

The SCLM composition is broadly correlated with crustal age and/or tectonic setting (e.g., Boyd and Mertman 1987; Boyd 1989, 1997; Griffin et al. 1998, 1999). Sometimes, however, the strong reworking during the Phanerozoic assembly of an orogenic belt may make older mantle components difficult to recognize (Griffin et al. 2000; Rudnick et al. 2004). Precambrian metamorphic rocks have been recently dated at 1900–707 Ma in the Western Tianshan (e.g., Hu et al. 1997, 2000; Chen et al. 1999, 2000). In the Eastern Tianshan,

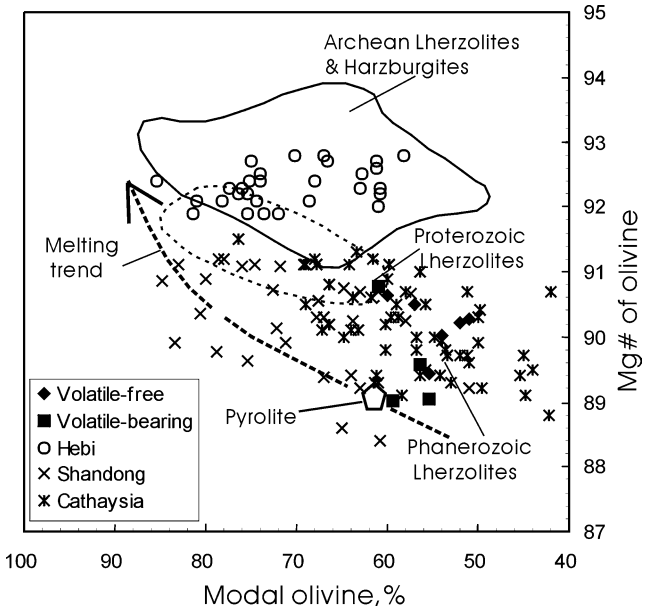

Fig. 12 $Mg^{\#}$ versus modal (%) olivine in Chinese peridotite xenoliths. Archean, Proterozoic and Phanerozoic areas are from Griffin et al. (1999); melting trend modified from Boyd (1989). Data sources: volatile-free and volatile-bearing from Tuoyun peridotites (this paper), Hebi (Zheng et al. 2001), Shandong including Shanwang and Qixia from Archean North China Craton (Zheng et al. 1998), Cathaysia including Mingxi, Qilin, Niutuoshan, Anyuan and Daoxian from Proterozoic Cathaysia Block (Qi et al. 1995; Xu et al. 2000; Zheng et al. 2004)

although early Paleozoic strata are relatively minor in comparison with late Paleozoic sequences, early Paleozoic (450–400 Ma) and even Neoproterozoic (1200–960 Ma; Hu et al. 1986) granitic rocks are widespread.

Two mica-bearing lherzolite xenoliths (T4p2, phlogopite-bearing, and T30, biotite-bearing) show very different features than those volatile-free and amphibole-bearing xenoliths. The relatively refractory nature for T4p2 (highest Fo) may represent old lithospheric mantle sample modified by hydrous potassic silicate melt. The extremely fertile lherzolite (T30, Fo down to 84) may show typical peridotite-melt reaction at high melt/rock ratios as stated by Zhang (2005). These highly fertile lherzolite xenoliths also occurred in the North China Craton (Xu et al. 1998). Therefore, although the SCLM beneath southwestern Tainshan is expected to be predominately Phanerozoic in nature, the minor population of moderately refractory peridotite xenoliths from Tuoyun may represent a relict Proterozoic component preserved at shallow levels (Zheng et al. 2004).

Mantle modification

Studies of secular changes in the density structure of the SCLM indicate that Archean and Proterozoic lithospheric sections in general are gravitationally stable and will tend to be preserved (Poudiom Djomani et al. 2001). Modification and replacement of the SCLM by tectonic

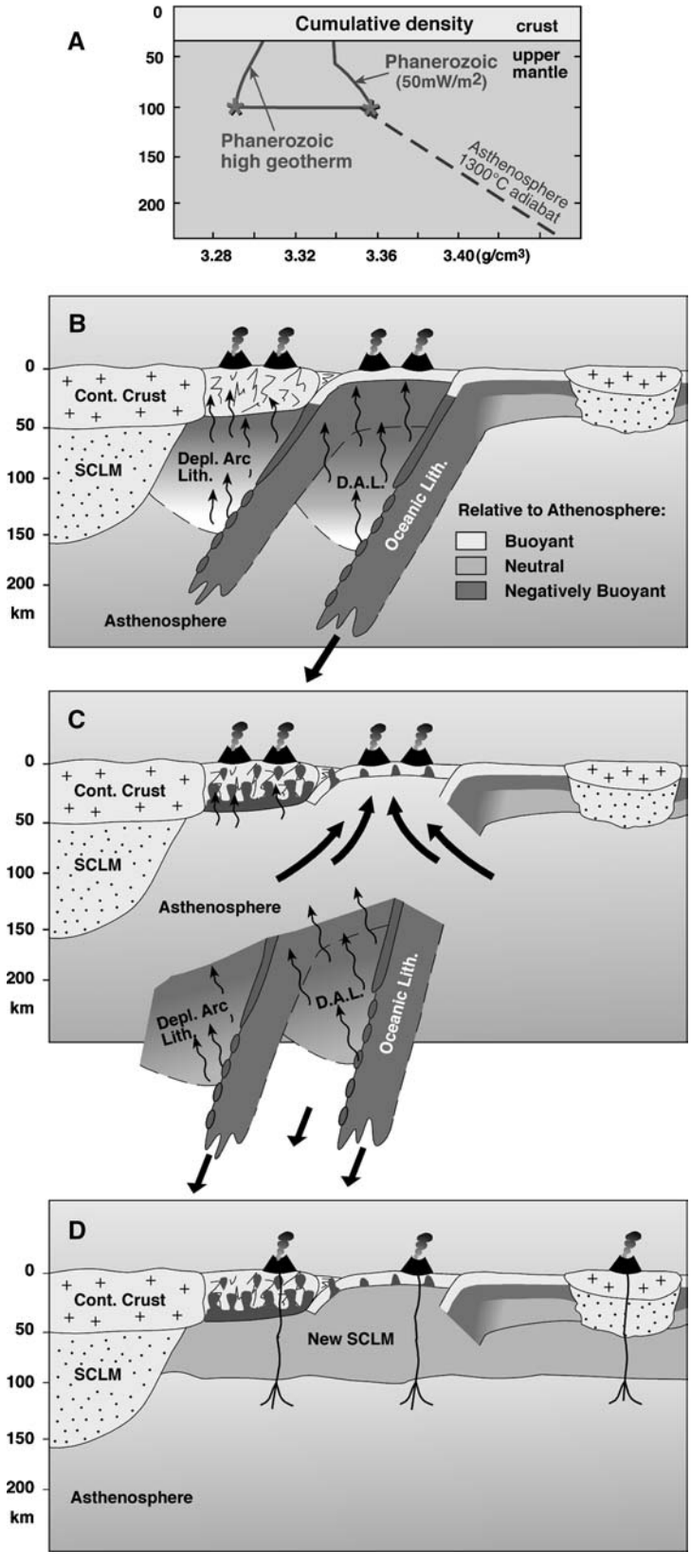

Fig. 13 Cartoon illustrating a model for the formation of the present SCLM beneath the Central Asia Orogenic Belt. **a** The cumulative density of a lithospheric column consisting of moderately depleted Phanerozoic mantle, on two geotherms: a higher one corresponding to the SE Australia geotherm and relevant to periods of active volcanism and a lower one representing thermal relaxation after the end of volcanism (after Poudiom Djomani et al. 2001). **b** Schematic density structure of a compound subduction system such as the CAOB, during its assembly (high geotherm, **a**); the negative buoyancy of the slabs is balanced by the increased buoyancy of the arc-related mantle wedges under high geothermal gradients. **c** Following cooling to a lower geotherm, the mantle wedges become negatively buoyant, leading to wholesale detachment of the newly accreted lithosphere; hot asthenosphere wells up to shallow depths, providing heat to melt the lower crust and produce granitoids; where microcontinental fragments (Zheng et al. 2006) are limited, most granitoids will have juvenile isotopic signatures. **d** Situation in late Mesozoic-Tertiary time: the upwelling asthenosphere has cooled to provide a new, thin and fertile SCLM, which is sampled by small-volume alkali basalt eruptions; local shallow remnants of older SCLM will provide xenoliths of more depleted peridotites

processes produce changes in the heat budget of the crust and are closely associated with continental collision, uplifting and magmatism (Griffin et al. 1998, 1999). The subduction of the Yangtze continent would add the crustal melt into the North China lithospheric mantle in Mesozoic (Zhang et al. 2002, 2004), especially along the

southern margin of the craton (Zheng et al. 2005). Yuan (1996) proposed a model based on seismic tomography to explain the dramatic change in the nature of the SCLM in the eastern part of the North China Craton during Mesozoic–Cenozoic times (Griffin et al. 1992, 1998; Menzies et al. 1993; Zheng 1999). In this model, old cold lithospheric mantle has been pulled apart during extension, and hot new material derived from the upwelling asthenosphere has risen along the major faults, spreading laterally in the upper part of the SCLM. The mantle beneath the TLFZ is dominantly Phanerozoic in character and is interpreted as newly accreted material that replaced the pre-existing older lithosphere through extension, thermal erosion and melt metasomatism (Zheng et al. 1998, 2004). These observations imply that the translithospheric Tanlu fault played an important part in the Mesozoic–Cenozoic replacement of the pre-existing Archean/Proterozoic lithospheric mantle. The upwelling of asthenospheric material resulted in irregular emplacement of hot fertile mantle material along the weak zones in the mantle.

A different model may be more appropriate for the Central Asia Orogenic Belt (CAOB). The CAOB is a broad collage of arcs, ocean remnants and microcontinental fragments, assembled during the closing of the Paleo-Tethys ocean in late Paleozoic time. The orogen experienced widespread and voluminous granitoid magmatism in Mesozoic time. Many of these igneous bodies have juvenile isotopic signatures (Jahn et al. 2000; Chen and Jahn 2002), implying derivation by melting of mafic lower crustal material underplated during the assembly of the orogen. This history can be understood in the context of the evolution in the density structure of such an accretionary orogen (Fig. 13a). During accretion, with active arc-related volcanism maintaining high geotherms, the lithosphere can maintain overall positive buoyancy relative to the underlying asthenosphere (Fig. 13b). However, when cooling sets in following the end of accretion and the cessation of volcanic activity, this newly accreted lithosphere will become negatively buoyant; even though the mantle wedge is highly depleted in Ca and Al, its Fe content remains high, leaving it with a relatively high density. In this situation, minor instabilities can trigger massive delamination of the young SCLM (Neil and Houseman 1999). Upwelling of the hot asthenosphere will provide the heat necessary to melt the lower crust (Fig. 13c), producing large volumes of granitoid magmatism; at the same time the upwelling asthenosphere will cool to form a new layer of fertile SCLM, like that observed in many xenolith suites from the CAOB (Figs. 8, 11, 12). Local volumes of older (and hence intrinsically buoyant) SCLM beneath microcontinental fragments will provide xenoliths of more refractory nature (Fig. 13d).

The present SCLM structure beneath the CAOB is interpreted as consisting of shallow thin remnants of older continental lithospheric mantle (also see Deng and Macdougall 1992) mixed with younger asthenospheric materials and deeper underplated "asthenospheric" material modified by minor further melting during upwelling (Griffin et al. 2000). The Tuoyun xenoliths show a higher proportion of fine-grained microstructure and a higher proportion of Cpx/Opx ratio than is seen in other parts of the CAOB. It also shows obvious enrichment in Ca and less obvious relics of the Proterozoic component than the latter. The inferred stronger mechanical and chemical modification of the Tuoyun mantle may be related to its location close to translithospheric faults such as the TF strike-slip fault (Fig. 1), which played a major role in controlling the strength of the mantle lithosphere and has channeled the upwelling mantle.

Conclusions

1. Mantle peridotite xenoliths from the Tuoyun basaltic rocks are characterized by a moderate depletion in basaltic components and metasomatic re-enrichment in incompatible elements compared with the spinel peridotite xenoliths from the Archean refractory mantle in Hebi and from the Phanerozoic fertile mantle in the area within the translithospheric fault zone of eastern China.
2. The large range of CaO/Al_2O_3 (0.9–3.5) in the whole rocks and the wide range of LREE/HREE (0.8–14.2), Ti/Eu (971–5,765) in clinopyroxene in the Tuoyun peridotites are interpreted as the cumulative effects of mantle metasomatism by carbonate and silicate melts through time.
3. Most of the Tuoyun peridotites experienced fractional melting of 5–8% and have more affinity to the Proterozoic Cathaysia block, and especially to the Phanerozoic East Central Asia Fold Belt with minor Proterozoic components, than to the Archean North China Craton. We suggest that the Tianshan mantle sampled by the Cretaceous Tuoyun basaltic rocks may contain Proterozoic relics, represented by some more refractory xenoliths, within a mainly Phanerozoic mantle generated in Mesozoic time.
4. A high proportion of fine-grained microstructures and high Cpx/Opx (Ca enrichment) in the Tuoyun mantle relative to the mantle beneath other parts of the CAOB (such as its eastern part) reflects its stronger mechanical and chemical modification, interpreted as related to its proximity to the TF strike-slip fault, which played a major role in controlling the strength of the mantle lithosphere and has channeled the upwelling mantle.

Acknowledgments This study was supported by the Nature Science Funding of China (40273001, 40425002 and 40521001), PCSIRT (IRT0441) and the ACILP AusAID Program and an ARC Discovery Project grant (SYO'R and W.L.G.). This is contribution no. 424 of the ARC National Key Centre for the Geochemical Evolution and Metallogeny of Continents (http://www.es.mq.edu.au/GEMOC/). We thank Drs. H.F. Zhang, Y.M. Pan and T.L. Grove for constructive reviews.

References

Afonichev NA, Vlasov HG (1984) Geologischeskaya karta kazakhstana Sredney Azii (so stratigraficheskimi kolonkami) Masshtab: 1:1,500,000 (Geological map of Kazakhstan and Middle Asia (with stratigraphic coluns), scale 1:1,500,000)

Allen MB, Windley BF, Zhang G, Zhao Z, Wang G (1991) Basin evolution within and adjacent to the Tianshan Range, NW China. J Geol Soc Lond 148:369–378

Allen MB, Windley BF, Zhang G (1992) Paleozoic collisional tectonics and magmatism of the Chinese Tianshan, central Asia. Tectonophysics 220:89–115

Blundy J, Dalton J (2000) Experimental comparison of trace element partitioning between clinopyroxene and melt in carbonate and silicate systems, and implications for mantle metasomatism. Contrib Mineral Petrol 139:356–371

Blusztajn J, Shimizu N (1994) The trace-element variations in clinopyroxenes from spinel peridotite xenoliths from southwest Poland. Chem Geol 111:227–243

Boyd FR (1989) Composition and distinction between oceanic and cratonic lithosphere. Earth Planet Sci Lett 96:15–26

Boyd FR (1997) Origin of peridotite xenoliths: major element consideration. In: Ranalli G, Ricci Lucchi F, Ricci CA, Trommosdorff T (eds) High pressure and high temperature research on lithosphere and mantle materials. University of Siena, Siena, pp 89–106

Boyd FR, Mertman SA (1987) Composition and structure of the Kaapvaal lithosphere, southern Africa. In: Mysen BO (ed) Magmatic processes: physicochemical principles. Geochemical Society, special publication 1, pp 13–24

Brey GP, Kohler T (1990a) Geothermobarometry in four-phase lherzolites I: experimental results from 10 to 60 kb. J Petrol 31:1313–1352

Brey GP, Kohler T (1990b) Geothermobarometry in four-phase lherzolites II: new thermobarometers and practical assessment of existing thermobarometers. J Petrol 31:1352–1378

Brookfield ME (2000) Geological development and Phanerozoic crustal accretion in the western segment of the southern Tien Shan (Kyrggzstan, Uzbokistan and Tajikistan). Tectonophysics 328:1–14

Carroll AR, Liang Y, Graham S, Xiao X, Hendrix MS, Chu J, McKnight CL (1990) Junggar basin, northwest China: trapped Late Paleozoic ocean. Tectonophysics 186:1–14

Chen B, Jahn BM (2002) Geochemical and isotopic studies of the sedimentary and granitic rocks of the Altay orogen of northwest China and their tectonic implications. Geol Mag 139:1–13

Chen CM, Lu HF, Jia D, Cai DS, Wu SM (1999) Closing history of the southern Tianshan oceanic basin, western China: an oblique collisional orogeny. Tectonophysics 302:23–40

Chen YB, Hu AQ, Zhang GX, Zhang QF (2000) Precambrian basement age and characteristics of Southwestern Tianshan: Zircon U–Pb geochronology and Nd–Sr isotopic compositions (in Chinese). Acta Petrol Sin 16(1):91–98

Chen SH, O'Reilly SY, Zhou XH, Griffin WL, Zhang GH, Sun M, Feng JL, Zhang M (2001) Thermal and petrological structure of the lithosphere beneath Hannuoba, Sino-Korean craton, China: evidence from xenoliths. Lithos 56:267–301

Chen J, Burbank DW, Scharer KM, Sobel E, Yin JH, Rubi C, Zhao RB (2002) Magnetochronology of the Upper Cenozoic strata in the Southwestern Chinese Tianshan: rates of Pleistocene folding and thrusting. Earth Planet Sci Lett 195:113–130

Coleman RG (1989) Continental growth of north China. Tectonics 8:621–636

Coltorti M, Bonadiman C, Hinton RW, Siena F, Upton BGJ (1999) Carbonatite metasomatism of the oceanic upper mantle: evidence from clinopyroxenes and glasses in ultramafic xenoliths of Grande Comore, Indian Ocean. J Petrol 40:133–165

Deng FL, Macdougall JD (1992) Proterozoic depletion of the lithosphere recorded in mantle xenoliths from Inner Mongolia. Nature 360:333–336

Dobresov GL, Zagruzina IA (1977) Young basaltoid igneous activity in the eastern Tianshan. Acad Sci USSR, Dokl, Earth Sci Sect 235:67–70

Eggler DH (1987) Solubility of major and trace elements in mantle metasomatic fluids: experimental constraints. In: Menzies MA, Hawkesworth CJ (eds) Mantle metasomatism. Academic Press Geology Series, London, pp 21–41

Fan WM, Zhang HF, Baker J, Jarvis KE, Mason PRD, Menzies MA (2000) On and off the North China: where is the Archean keel? J Petrol 41:933–950

Frey FA, Prinz M (1978) Ultramafic inclusions from San Carlos, Arizona: petrologic and geochemical data bearing on their petrogenesis. Earth Planet Sci Lett 38:129–176

Gao J, He G, Li M, Xiao X, Tang Y, Wang J, Zhao M (1995) The mineralogy, petrology, metamorphic PTDt trajectory and exhumation mechanism of blueschists, south Tianshan, northwest China. Tectonophysics 250:151–168

Gao J, Li MS, Xiao XC, Tang YQ, He GQ (1998) Paleozoic tectonic evolution of the Tianshan Orogen, northwestern China. Tectonophysics 287:213–231

Glaser SM, Foley SF, Günther D (1999) Trace element compositions of minerals in garnet and spinel peridotite xenoliths from the Vitim volcanic field, Transbaikalia, eastern Siberia. Lithos 48:263–285

Graham SA, Brassell S, Carroll AR, Xiao X, Demaison G, Mcknight CL, Liang Y, Chu J, Hendrix MS (1990) Characteristics of selected petroleum source rocks, Xinjiang Uygar autonomous region, northwest China. Am Assoc Petrol Geol Bull 74:493–512

Griffin WL, O'Reilly SY, Ryan CG (1992) Composition and thermal structure of the lithosphere beneath South Africa, Siberia and China: proton microprobe studies. In: International symposium on Cenozoic volcanic rocks and deep-seated xenoliths of China and its environs, Beijing, p 20

Griffin WL, O'Reilly SY, Ryan CG, Gaul O, Ionov DI (1998) Secular variation in the composition of subcontinental lithospheric mantle: geophysical and geodynamic implications. In: Braun J, Dooley JC, Goleby BR, van der Hilst RD, Klootwijk CT (eds) Structure and evolution of the Australian Continent. Geodynamics, vol 26. American Geophysical Union, Washington, pp 1–26

Griffin WL, O'Reilly SY, Ryan CG (1999) The composition and origin of sub-continental lithospheric mantle. In: Fei Y, Berka CM, Mysen BO (eds) Mantle petrology: field observations and high-pressure experimentation, pp 13–45

Griffin WL, O'Reilly SY, Ionov DA, Poudiom Djomani YH, Malkovets VG (2000) Mantle evolution in the East Central Asia Orogenic Belt: heat sources for granite generation. Abstract of IGCP, Wurumuqi

Han BF, Wang XC, He GQ (1998) Discovery of upper mantle and lower crust xenolith in early Cretaceous volcanic rock from southwest Tianshan (in Chinese). Chin Sci Bull 43:2544–2547

Harte B (1977) Chemical variations in upper mantle nodules from southern African kimberlites. J Geol 85:279–288

Hart SR, Zindler A (1986) In search of bulk Earth composition. Chem Geol 57:247–267

Hellebrand E, Snow JE, Dick HJB, Hofmann AW (2001) Coupled major and trace elements as indicators of the extent of melting in mid-ocean-ridge peridotites. Nature 410:677–681

Hendrix MS, Graham SA, Carroll AR, Sobel ER, McKnight CL, Schulein BJ, Wang Z (1992) Sedimentary record and climatic implications of recurrent deformation in the Tianshan: evidence from Mesozoic strata of the north Tarim, South Junggar and Turpan basins, northwest China. Geol Soc Am Bull 104:53–79

Hendrix MS, Dumitru TA, Graham SA (1994) Late Oligocene–early Miocene unroofing in the Chinese Tian Shan: an early effect of the India–Asia collision. Geology 22:487–490

Hu AQ, Zhang JB, Zhang ZG, Zhao DJ, Liu JY, Yang SZ, Peng JH, Zhou W (1986) U–Pb age and evolution of Precambrian metamorphic rocks of Middle Tianshan uplift zone eastern Tianshan, China (in Chinese). Geochemica 23:23–35

Hu AQ, Wang ZG, Tu GZ (1997) Geological evolution and diagenic and metallogenetic regularity in Northern Xinjiang (in Chinese). Science Press, Beijing, pp 9–105
Hu AQ, Jahn BM, Zhang GX, Chen YB, Zhang QF (2000) Crustal evolution and Phanerozoic crustal growth in northern Xinjiang: Nd isotopic evidence. Part I. Isotopic characterization of basement rocks. Tectonophysics 328:15–51
Ionov DA (2002) Mantle structure and rifting processes in the Bailkal-Mongolia region: geophysical data and evidence from xenoliths in volcanic rocks. Tectonophysics 351:41–60
Ionov DA, Prikhod'ko VS, O'Reilly SY (1995) Peridotite xenoliths in alkali basalts from the Sikhote-Alin, southeastern Siberia, Russia: trace-element signatures of mantle beneath a convergent continental margin. Chem Geol 120:275–294
Ionov DA, O'Reilly SY, Griffin WL (1997) Volatile-bearing minerals and lithophile trace elements in the upper mantle. Chem Geol 141:153–184
Ionov DA, O'Reilly SR, Griffin WL (1998) A geotherm and lithospheric section for the Central Mongolia (Tariat Region). In: Flower MFJ, Chung SL, Lo CH, Lee TY (eds). Mantle dynamics and plate interactions in East Asia. AGU geodynamics series 27, pp 127–153
Ionov DA, Griffin WL, O'Reilly SY (1999) Off-craton garnet and spinel peridotite xenoliths from Dsun-Bussular, SE Mongolia. In: Proceedings of the 7th international Kimberlite conference, Red Roof Design, Cape Town, pp 383–390
Ionov DA, Ashchepkov I, Jagoutz E (2005) The provenance of fertile off-carton lithospheric mantle: Sr–Nd isotope and chemical composition of garnet and spinel peridotite xenoliths from Vitim, Siberia. Chem Geol 217:41–75
Jahn BM, Wu FY, Chen B (2000) Massive granitoid generation in Central Asia: Nd isotope evidence and implication for continental growth in the Phanerozoic. Eoisodes 23:82–92
Jonson KTM, Dick HJB, Shimizu N (1990) Melting in the oceanic upper mantle: an ion microprobe study of diopside in abyssal peridotites. J Geophys Res 95:2661–2678
Klemme S, van der Laan SR, Foley SF, Gunther D (1995) Experimentally determined trace and minor element partitioning between clinopyroxene and carbonatite melt under upper mantle conditions. Earth Planet Sci Lett 133:439–448
Kopylova MG, O'Reilly SY, Genshaft YS (1995) Thermal state of the lithosphere beneath Central Mongolia: evidence from deep-seated xenoliths from the Shavaryn-saram volcanic center in the Tariat depression, Hangai, Mongolia. Lithos 36:243–255
Le Maitre RW (1982) A classification of igneous rocks and glossary of terms. Blackwell, London
Litasov KD, Foley SF, Litasov YD (2000) Magmatic modification and metasomatism of the subcontinental mantle beneath the Vitim volcanic field (East Siberia): evidence from trace element data on pyroxenite and peridotite xenoliths from Miocene picrobasalt. Lithos 54:83–114
McDonough WF, Sun SS (1995) The composition of the Earth. Chem Geol 120:223–253
Meen JK (1987) Mantle metasomatism and carbonates: an experimental study of a complex relationship. Geol Soc Am Spec Paper 215, pp 91–100
Menzies MA, Fan W, Zhang M (1993) Palaeozoic and Cenozoic lithoprobes and loss of >120 km of Archean lithosphere, Sino-Korean craton, China. In: Prichard HM, Alabaster T, Harris NBW, Neary CR (eds) Magmatic processes and plate tectonics. Geological Society, special publication 76, pp 71–81
Molnar P, Tapponnier P (1975) Cenozoic tectonics of Asia: effects of a continental collision. Science 189:419–426
Neil EA, Houseman GA (1999) Rayleigh–Taylor instability of the upper mantle and its role in intraplate orogeny. Geophys J Int 138:89–107
Nelson MR, Mccafferey R, Molnar P (1987) Source parameters for eleven earthquakes in the Tien Shan, central Asia: determined by P and S waveform inversion. J Geophys Res 92:12629–12648
Neumann ER, Wulff-Pedersen E, Pearson NJ, Spencer EA (2002) Mantle xenoliths from Tenerife (Canary Islands): evidence for reactions between mantle and silicic carbonatite melts inducing Ca metasomatism. J Petrol 43:825–857
Norman MD (1998) Melting and metasomatism in the continental lithosphere: laser ablation ICPMS analysis of minerals in spinel lherzolites from eastern Australia. Contrib Mineral Petrol 130:240–255
Norman MD, Pearson NJ, Sharma A, Griffin WL (1996) Quantitative analysis of trace elements in geological materials by laser ablation ICPMS: instrumental operating conditions and calibration values of NIST glasses. Geostand Newsl 20:247–261
O'Reilly SY, Chen D, Griffin WL, Ryan CG (1996) Minor element in olivine from spinel lherzolite xenoliths: implications for thermobarometry. Mineral Mag 61:257–269
Pouchou JL, Pichoir F (1984) A new model for quantitative X-ray microanalysis. Part 1: application to the analysis of homogeneous samples. Recherche Aerospatial 5:13–38
Poudiom Djomani YH, O'Reilly SY, Griffin WL (2001) The density structure of subcontinental lithosphere through time. Earth Planet Sci Lett 184:605–621
Preß S, Witt G, Seck HA, Eonov D, Kovalenko VI (1986) Spinel peridotite xenoliths from the Tariat Depression, Mongolia. I: major element chemistry and mineralogy of a primitive mantle xenolith suite. Geochim Cosmochim Acta 50:2587–2599
Qi Q, Taylor LA, Zhou X (1995) Petrology and geochemistry of mantle peridotite xenoliths from Southeastern China. J Petrol 36:55–79
Rudnick RL, McDonough WF, Chappell W (1993) Carbonatite metasomatism in the northern Tanzanian mantle: petrographic and geochemical characteristics. Earth Planet Sci Lett 114:463–475
Rudnick RL, Gao S, Ling WL, Liu YS, McDonough WF (2004) Petrology and geochemistry of spinel peridotite xenoliths from Hanuoba and Qixia, North China Craton. Lithos 77:297–317
Sachtleben T, Seck HA (1981) Chemical control of Al-solubility in orthopyroxene and its implications on pyroxene geothermometry. Contrib Mineral Petrol 78:157–165
Sengör AMC, Natal'in BA (1996) Paleotectonics of Asia: fragments of a synthesis. In: Yin A, Harrison TM (eds) The tectonic evolution of Asia. Cambridge University Press, New York, pp 486–640
Shi YS, Lu HF, Jia D, Cai DS, Wu SM, Chen CM, Howell DG, Valin ZC (1994) Paleozoic plate-tectonic evolution of the Tarim and western Tianshan regions, western China. Int Geol Rev 36:1058–1066
Sobel ER, Arnaud N (2000) Cretaceous-Paleogene basaltic rocks of the Tuyon basin, NW China and the Kyrgyz Tian Shan: the trace of a small plume. Lithos 50:191–215
Stalder R, Foley SF, Brey GP, Horn I (1998) Mineral-aqueous fluid partitioning of trace elements at 900–1200 C and 3.0–5.7 GPa: new experimental data for garnet, clinopyroxene, and rutile, and implications for mantle metasomatism. Geochim Cosmochim Acta 62:1781–1801
Stosch HG, Lugmair GW, Kovalenko VI (1986) Spinel peridotite xenoliths from the Tariat depression Mongolia. II: geochemistry and Nd and Sr isotopic composition and their implications for the evolution of the subcontinental lithosphere. Geochim Cosmochim Acta 50:2601–2614
Sun SS, McDonough WF (1989) Chemical and isotopic systematics of oceanic basalts: implications for mantle composition and processes. In: Saunders AD, Norry MJ (eds) Magmatism in the ocean basins. Special Publication of the Geological Society of London 42, pp 313–346
Tapponnier P, Molnar P (1979) Active faulting and Cenozoic tectonics of the Tianshan, Mongolia and Baykal region. J Geophys Res 84:3425–3459
Wells PRA (1977) Pyroxene thermometry in simple and complex systems. Contrib Mineral Petrol 62:129–139

Wiechert U, Ionov DA, Wedepohl KH (1997) Spinel peridotite xenoliths from the Atsagin-Dush volcano, Dariganga lava plateau, Mongolia: a record of partial melting and cryptic metasomatism in the upper mantle. Contrib Mineral Petrol 126:345–364

Wilshire HG, Shervais JW (1975) Al-augite and Cr-diopside ultramafic xenoliths in basaltic rocks from western United States. Phys Chem Earth 9:257–272

Windley BF, Allen MB, Zhang C, Zhao ZY, Wang GR (1990) Paleozoic accretion and Cenozoic re-deformation of the Chinese Tien Shan range, Central Asia. Geology 18:128–131

Witt-Eickschen G, Seck HA (1991) Solubility of Ca and Al in orthopyroxene from spinel peridotite: an improved version of an empirical geothermometer. Contrib Mineral Petrol 106:431–439

Xiao XC, Tang YQ, Feng YM (1992) Tectonics of North Xinjiang and its adjacent region (in Chinese). Geological Publishing House, Beijing, pp 55–60

Xu YG, Menzies MA, Mattery DP, Lowry D (1996) The nature of the lithospheric mantle near the Tancheng-Lujiang fault, China: an integration of texture, chemistry and isotopes. Chem Geol 134:67–81

Xu XS, O'Reilly SY, Griffin WL, Zhou X, Huang X (1998) The nature of the Cenozoic lithosphere at Nushan, Eastern China. In: Flower MFJ, Chung SL, Lo CH, Lee TY (eds) Mantle dynamics and plate interactions in East Asia. AGU geodynamics series 27:167–195

Xu XS, O'Reilly SY, Griffin WL, Zhou X (2000) Genesis of young lithospheric mantle in southeastern China: a LAM-ICPMS trace element study. J Petrol 40:111–148

Yaxley GM, Green DH, Kamenetsky V (1998) Carbonatite metasomatism in the southeastern Australia lithosphere. J Petrol 39:1917–1930

Yuan XC (1996) Atlas of geophysics in China. Geological Publishing House, Beijing

Zangana NA, Downes H, Thirlwall MF, Marriner GF, Bea F (1999) Geochemical variation in peridotite xenoliths and their constituent clinopyroxenes from Ray Pic (French Massif Central): implications for the composition of the shallow lithospheric mantle. Chem Geol 153:11–35

Zhang HF (2005) Transformation of lithospheric mantle through peridotite-melt reaction: a case of Sino-Korean craton. Earth Planet Sci Lett 237:768–780

Zhang M, Suddaby P, O'Reilly SY, Norman M, Qiu JX (2000) Nature of the lithospheric mantle beneath the eastern part of the Central Asia fold belt; mantle xenolith evidence. Tectonophysics 328:131–156

Zhang HF, Sun M, Zhou XH, Fan WM, Zhai MG, Yin JF (2002) Mesozoic lithosphere destruction beneath the North China Craton: evidence from major-, trace-element and Sr–Nd–Pb isotope studies of Fangcheng basalts. Contrib Mineral Petrol 144:241–253

Zhang HF, Sun M, Zhou MF, Fan WM, Zhou XH, Zhai MG (2004) Highly heterogeneous late Mesozoic lithospheric mantle beneath the North China Craton: evidence from Sr–Nd–Pb isotopic systematics of mafic igneous rocks. Geol Mag 141:55–62

Zheng JP (1999) Mesozoic–Cenozoic mantle replacement and lithospheric thinning, East China (in Chinese). China University of Geosciences Press, Wuhan, p 126

Zheng JP, O'Reilly SY, Griffin WL, Lu FX, Zhang M (1998) Nature and evolution of Cenozoic lithospheric mantle beneath Shandong peninsula, Sino-Korean craton. Int Geol Rev 40:471–499

Zheng JP, O'Reilly SY, Griffin WL, Lu FX, Zhang M, Pearson NJ (2001) Relics of refractory mantle beneath the eastern North China block: significance for lithosphere evolution. Lithos 57:43–66

Zheng JP, O'Reilly SY, Griffin WL, Zhang M, Lu FX, Liu GL (2004) Nature and evolution of Mesozoic–Cenozoic lithospheric mantle beneath the Cathaysia block, SE China. Lithos 74:41–65

Zheng JP, Sun M, Zhou MF, Robinson P (2005) Trace elemental and PGE geochemical constraints of Mesozoic and Cenozoic peridotitic xenoliths on lithospheric evolution of the North China Craton. Geochim Cosmochim Acta 69:3401–3418

Zheng JP, Griffin WL, O'Reilly SY, Zhang M, Liou JG, Norman P (2006) Granulite xenoliths and their zircons, Tuoyun, NW China: insights into southwestern Tianshan lower crust. Precam Res (in press)

Zhou Q, Zheng J (1992) Structural analysis. In: Petroleum geology of Tarim Basin (in Chinese). Science Press, Beijing, p 144

Zinngrebe E, Foley SF (1995) Metasomatism in mantle xenoliths from Gees, west Eifel, Germany: evidence for the genesis of calc-alkaline glasses and metasomatic Ca-enrichment. Contrib Mineral Petrol 122:79–96

Zorin YA (1999) Geodynamics of the western part of Monolia-Okhotsk collisional belt, Trans-Baikal region (Russia) and Mongolia. Tectonophysics 306:33–56